DOE/MC/29116--3956
(DE95000047)

# Novel Mass Spectrometric Instrument for Gaseous and Particulate Characterization and Monitoring

**Final Report**
**September 1992 - August 1994**

Michael J. Coggiola
Christopher H. Becker
Clyde L. Witham

October 1994

Work Performed Under Contract No.: DE-AC21-92MC29116

For

U.S. Department of Energy
Office of Environmental Management
Office of Technology Development
Washington, DC

U.S. Department of Energy
Office of Fossil Energy
Morgantown Energy Technology Center
Morgantown, West Virginia

By
SRI International
Menlo Park, California

# DISCLAIMER



This report has been reproduced directly from the best available copy.

Available to DOE and DOE contractors from the Office of Scientific and Technical Information, P.O. Box 62, Oak Ridge, TN 37831; prices available from (615) 576-8401.

Available to the public from the U.S. Department of Commerce, Technology Administration, National Technical Information Service, Springfield, VA 22161, (703) 487-4650.

DOE/MC/29116--3956
(DE95000047)
Distribution Category UC-906

# Novel Mass Spectrometric Instrument for Gaseous and Particulate Characterization and Monitoring

## Final Report
## September 1992 - August 1994

Michael J. Coggiola
Christopher H. Becker
Clyde L. Witham

Work Performed Under Contract No.: DE-AC21-92MC29116

For

U.S. Department of Energy
Office of Environmental Management
Office of Technology Development
1000 Independence Avenue
Washington, DC 20585

U.S. Department of Energy
Office of Fossil Energy
Morgantown Energy Technology Center
P.O. Box 880
Morgantown, West Virginia 26507-0880

By

SRI International
333 Ravenswood Avenue
Menlo Park, California 94025

October 1994

## CONTENTS

## TABLES

## FIGURES

## EXECUTIVE SUMMARY

Under contract DE-AC-21-92MC29116, SRI International is developing a unique new instrument that will be capable of providing real-time (<1 minute), quantitative, chemical characterization of gaseous and particulate pollutants generated from DOE waste cleanup activities. The instrument will be capable of detecting and identifying volatile organic compounds, polynuclear aromatic hydrocarbons, heavy metals, and transuranic species released during waste cleanup activities. The instrument will be unique in its ability to detect and quantify in real-time these diverse pollutants in both vapor and particulate form.

The instrument being developed under this program consists of several major components: (1) an isokinetic sampler capable of operating over a wide range of temperatures (up to 500 K) and flow rates; (2) a high pressure to low pressure transition and sampling region that efficiently separates particles from vapor-phase components for separate, parallel analyses; (3) two small mass spectrometers, one optimized for organic analysis using a unique field ionization source and one optimized for particulate characterization using thermal pyrolysis and electron-impact ionization (EI); and (4) a powerful personal computer for control and data acquisition.

The function of the sampler is to obtain a sufficient and representative quantity of air pollutants from a wide range of waste cleanup activities, both vapor and particulate. In addition, the sampler must deliver the vapors and particles to the detection instrument with minimal material loss. The pressure transition region serves multiple functions: (1) it focuses the particles into a "beam" toward the center of the gas flow by momentum separation, (2) it efficiently separates the particulate beam from the vapor stream, allowing independent chemical analyses of particles and vapors, and (3) it provides the first stage of pressure reduction between the ambient atmosphere and the lower pressure ($10^{-4}$–$10^{-5}$ Torr) region of an ion trap mass spectrometer.

Chemical analysis of the volatile organic species and the polynuclear aromatic hydrocarbons is typically accomplished by first enriching their concentration using a dimethylsilicone rubber membrane separator and then analyzing their composition with field ionization mass spectrometry (FIMS). FIMS is a soft ionization method that is ideally suited to the chemical characterization of complex mixtures of organic compounds. Also available will be an alternative direct inlet of vapors bypassing the membrane and use of electron impact (EI) ionization, for comparisons with the membrane inlet and field ionization. Use of EI will permit monitoring of various small inorganic molecules as well, such as $NO_x$ and $SO_x$.

The direct sampling method and differential vacuum pumping allow particulate pollutants to be readily introduced into another ion trap mass spectrometer. Volatilization of particles on a heated surface within the volume of the ion trap followed by the complete and quantitative mass spectrometric analysis of the resulting vapors will yield the detailed information required to monitor waste cleanup activity. Estimates of the instrument design and performance parameters show that a single 0.3-μm-diameter particle will provide a signal level sufficient for complete analysis. All these operations are under the control of the data acquisition computer.

The overall goal of this effort is to develop and demonstrate an instrument that can provide real-time, part-per-billion detection sensitivity for important pollutant species generated by DOE waste cleanup activities. Initially, the instrument will be developed for targeted use in conjunction with the K-1435 Toxic Substances Control Act (TSCA) incinerator at the Oak Ridge National Laboratory K-25 site. Ultimately, the instrument will be designed to operate in the field at any cleanup site, located close to the stack or process vent, providing the plant operations personnel with real-time information and alarm capabilities. In addition, this instrument will be very broadly applicable for cleanup or sampling, for example, any time contaminated soil is moved or disturbed.

Because of the versatility and analytical power of this instrument, commercialization for a wide variety of applications in monitoring and control will be important.

The instrument relies on both commercially available technology, including a simple laser scattering particle detector, an ion trap mass spectrometer and a membrane permeator, and unique technologies developed by our organization in the areas of field ionization mass spectrometry and high-temperature sampling. The instrument is projected to be easily transportable with minimal utility requirements, making it ideal for deployment at a wide variety of DOE waste sites. Moreover, the straightforward design and use of proven technologies will result in an instrument of very high reliability and sensitivity that can be ready for actual field testing and use within two to three years. Other applications within the DOE include (1) monitoring of the vitrification processes used to solidify high-level waste (HLW), (2) real-time chemical analysis of storage tank offgassing, and (3) characterization of tropospheric particulates that are significant to DOE's Atmospheric Radiation Measurement (ARM) program.

This report details the technical accomplishments achieved during the first phase of the research effort.

# 1 INTRODUCTION

The goals of the Office of Technology Development, as outlined by the director of the Environmental Restoration and Waste Management Program (EM), Leo Duffy, in the 1991 appropriations hearings, include conducting an aggressive technology development program for waste management, waste minimization, waste treatment, storage, and disposal of waste. These goals will be accomplished through the development of more effective remediation technology to reduce occupational and public exposure. We are developing a method for monitoring airborne emissions from the TSCA plant at Oak Ridge to provide real-time, accurate, and inexpensive data on the emission of hazardous organic and inorganic chemicals in both gaseous and particulate form and to assist DOE in maintaining its ambitious schedules and in overcoming significant scientific limitations of its current monitoring technologies.

In May 1988 under the Comprehensive Environmental Response, Compensation, and Liability Act (CERCLA), Oak Ridge National Laboratory (ORNL) established a timetable remedial investigation/feasibility study, and a Federal Facility Agreement is being negotiated with the Environmental Protection Agency and the Tennessee Department of Health and Environment. As a result, work has begun on inactive waste sites at ORNL to excavate and isolate wastes in compliance with current standards. In addition, ORNL must comply with the Resource Conservation and Recovery Act (RCRA), which regulates generation, transportation, treatment, storage, and disposal of hazardous wastes and corrective action following releases to the environment of hazardous wastes from active facilities.

Environmental restoration activities at DOE-ORO sites and facilities, such as K-25 and Y-12, are conducted to meet location, contaminant, and action-specific requirements imposed by statutes and regulations and to implement guidance and agreements. These activities typically follow a phased approach that includes public involvement throughout the process.

The Oak Ridge Operations Office is responsible for the environmental remediation and restoration activities at the Oak Ridge, Y-12 and K-25 facilities. Support of both the Department of Energy's and the State of Tennessee's commitment to environmental issues is a vital concern of the Oak Ridge site's workforce and management structure. Through advances in technology, the environmental remediation and restoration efforts may be accomplished at less cost and with a decreased impact on the surrounding communities.

# 2 BACKGROUND

## 2.1 OAK RIDGE K-25 SITE

The Oak Ridge K-25 site is located 13 miles west of Oak Ridge. Until the summer of 1985, when the gaseous diffusion process was shut down, the mission of the K-25 site was $^{235}U$ enrichment of uranium hexafluoride ($UF_6$) for eventual use as a fuel in nuclear reactors. Typical facilities included the feed system and separate systems for collecting the product and the waste (tails) stream. The purging of contaminants from the product stream required the use of large amounts of alumina and sodium fluoride. A number of compounds were used for the clarification of coolant water, and hexavalent chromium, zinc, and phosphate were used to inhibit corrosion of heat transfer equipment. Support facilities produced solutions that required concentration and

recovery plus some residual that was discarded and buried. Laboratory sample residues and obsolete chemical reagents, spent chemicals, and contaminated equipment were candidates for discard. Sludges from chemical wastes contained hazardous materials, including chromium, copper, lead, mercury, naphthalene, and zinc. Wastes buried at the K-25 site include low-level radioactive solid waste, mixed chemical waste, and radioactive and nonradioactive classified materials. Uranium was released into the air, surface water, and on-site land disposal.

Waste management activities at the K-25 site are increasing. Low-level radioactive waste from other DOE-Oak Ridge Operations (ORO) sites is now being placed in interim storage facilities in the K-25 site building vaults until final disposition strategy is identified. Also, polychlorinated biphenyl (PCB) wastes began arriving from other DOE-ORO sites in 1987 for future incineration in the new K-1435 Toxic Substances Control Act incinerator.

Making an analogy, it is well established that heavy metals are present in the stack emissions of coal-fired power plants. Considerable research in this area has identified every naturally occurring element in coal fly ash, with concentrations ranging from percents to parts-per-million and below. In the case of coal combustion, these heavy metals are present in the feedstock, whereas in the process stream of a waste cleanup facility, many heavy metals will be present at high concentrations as part of the original waste material. Although a number of the naturally occurring elements are of minor concern, many of the heavy metals, such as mercury, lead, cadmium, arsenic, chromium, and uranium, pose significant health risks to humans. Additionally, the transuranic elements such as plutonium are of particular concern due to their extreme toxicity as respirable particles. Many other elements, both radioactive and nonradioactive, also pose health and safety risks. Included in this category are particles containing beryllium, iodine, and cesium.

By analogy with the known distribution of heavy metals within airborne particles generated by coal-fired power plants, it is reasonable to conclude that significant levels of heavy metals and hazardous inorganic contamination can be unknowingly discharged from process vent stacks in the particulate form. Maintaining a high degree of safety and control over cleanup activities at waste sites containing these materials requires a monitoring instrument that can provide real-time, quantitative measurements of levels of important elements at any point within the process. Particular attention must be given to effluent discharge to the atmosphere via vents and stacks to prevent any release of hazardous by-products of the cleanup activities.

In addition to the heavy metal and inorganic emissions, a very wide range of volatile organic (VOCs) will be produced and emitted from any waste cleanup plants, including polycyclic aromatic hydrocarbons (PAHs), heterocyclic nitrogen and sulfur species, and polychlorinated biphenyls (PCBs). Many of these VOCs are known or suspected carcinogens whose levels must also be controlled. Unlike the metals and inorganic species, many of the organic compounds found in the gaseous effluent of waste cleanup facilities will include materials not initially present in the waste stream. For example, many PAHs are formed during the incomplete combustion of simple organic wastes. As with metals and inorganics, the organic pollutants can be released in both the vapor and particulate forms. Thus, a versatile real-time instrument for determining VOC levels is required to allow plant operators to monitor and regulate stack emissions of these hazardous species.

Any real-time waste cleanup process monitor should be capable of simultaneously measuring numerous important chemical species, both organic and inorganic, present as vapors and particles. Although very sophisticated monitoring technologies are currently under development that make use of optical, electrochemical, and microsensor methods, none yet offers quantitative chemical characterization of both vapor phase and particulate air pollutants. Moreover, most of these sophisticated sensors are capable of detecting only one or two specific chemical species, thereby requiring that many separate sensors be integrated to perform the necessary monitoring and control functions. Such multisensor systems will often be technologically more complex and less reliable than a single, multifunctional instrument as well as more costly to develop, manufacture, operate, and maintain.

The most universal analytical technique available for monitoring a broad range of chemical species is mass spectrometry. If mass spectrometry is to be used, however, the sampled materials must be vaporized and ionized before analysis. The ionization method must be carefully chosen to prevent preferential, or nonstatistical, ionization while providing adequate and stable signal levels. Even before the effluent can be ionized, it must be sampled and transported from the stack or process stream to the ionizer. In the case of a waste cleanup plant such as the K-1435 TSCA incinerator at the DOE-Oak Ridge Operations site, the sampled effluent will consist of vapors and particles. Thus, the development of an appropriate sampler will be a critical aspect of this effort. Most of the heavy metals, for example, will not appear in vapor form, but will be incorporated into particles of varying sizes. Not only must these particles be efficiently sampled, they must also be separated from the vapor component and then completely vaporized to provide the requisite composition information. At the same time, the sampled vapors, including the organic species of interest, must be isolated and efficiently detected. No single *instrumental* technique (FTIR, ICP-AES, ICP-MS, GC, GC-MS, LIF) is capable of simultaneously detecting both organic and inorganic species in vapor and particulate forms. However, a single *instrument* consisting of two closely integrated detectors that share a common sampler can provide this critical analytical capability.

## 2.2 OTHER APPLICATIONS

Although the primary application for which this instrument is being development is the monitoring of stack emissions from waste incinerators such as the TSCA, other DOE-related applications are readily apparent. Two examples have been discussed with DOE EM headquarters staff: (1) real-time, online monitoring of the vitrification processes that will be used to enable the long-term storage of hazardous liquid waste (HLW), and (2) real-time chemical speciation of the solid waste tank core samples from Hanford. While each of these applications would require some design and operational modifications of the ion trap instrument, the technology being developed under the current program would form their fundamental underlying foundation.

### 2.2.1 Vitrification Monitoring

New technologies are currently being developed to treat and immobilize HLW for permanent storage. Among these processing methods is vitrification. Proposed schematics of large-scale vitrification plants show a strong emphasis on exhaust treatment methods to reduce particulate emissions. If these vitrification plants are implemented, they will require the installation and use of a considerable array of online, real-time monitoring instrumentation. The ion trap system being developed under the present program offers an ideal platform upon which to base instrumentation that will be needed to monitor the vitrification process. The same core instrument could be used at several points in the process to monitor the composition of flyash in the baghouse, particulates before and after HEPA filters, residual species in the exhaust stream following scrubbers, and finally, stack emissions. In each case, a different sampling probe is all that is required to utilize the same basic instrument.

### 2.2.2 Waste Tank Core Sample Characterization

At the suggestion of Al Tardiff (EM-50), we have initiated discussions with the staff of the Laser-Abalation/Mass-Spectrometry (LA/MS) development group at Pacific Northwest Laboratory (PNL). The LA/MS effort is part of the larger MARS program that is working toward an accelerated characterization of the Hanford waste storage tanks under the EM-50 Characterization, Monitoring and Sensor Technology Integrated Program. A major portion of LA/MS technology being developed by PNL is designed to (1) produce particulates directly from solid core samples using laser ablation, (2) entrain the particulates in a carrier gas flow, and (3) perform chemical

analysis using mass spectrometry. The PNL group envisions using several different analytical instruments to determine both the elemental speciation as well as the chemical speciation of the particulates. By use of the first two stages of PNL's instrument (laser ablation and particulate transport in a carrier gas stream), solid waste tank core samples could be directly transformed into particulates that would be suitable for real-time chemical analysis by the ion trap mass spectrometer instrument. Thus, the SRI ion trap instrument and the PNL LA/MS front end are complementary technologies that will provide rapid chemical characterization of the Hanford storage tank contents.

### 2.2.3 Atmospheric Radiation Measurement (ARM) Program

The ARM Program is administered by the Office of Energy Research under the Office of Health & Environmental Research as part of the Environmental Sciences Division of DOE. Under the ARM program, DOE funds the development and deployment of new instruments designed to obtain environmentally significant information about upper atmospheric aerosols that are generated by fossil fuel combustion. The instrument that is being developed under the present program would have direct applicability to the ARM program by providing real-time, *in situ* sampling and analysis of tropospheric aerosols. Knowledge of the chemical composition of aerosol particles is required for the modeling and understanding of radiative processes in the Earth's atmosphere.

A related atmospheric monitoring program directed by NASA is the Subsonic Assessment Program (SASS) within the Atmospheric Effects of Aviation Project (AEAP). Recently, SRI has proposed to develop an instrument for the SASS mission that would also provide real-time chemical speciation of tropospheric aerosols. The instrument is similar in concept to that proposed here, and would be well suited for use on the ARM program. In a letter dated April 27, 1994, Wesley L. Harris, Associate Administrator for Aeronautics at NASA headquarters, notified SRI that NASA intends to fund the SASS development effort. Under NASA's present schedule, the SASS instrument would be deployed on a Spring, 1996 mission using their DC-8 aircraft.

## 3 ACCOMPLISHMENTS

The goals of this research program are to develop, demonstrate, and field test a real-time monitoring instrument capable of providing quantitative chemical information on the vapor and particulate emissions produced during the incineration of toxic waste. The Phase 1 effort was divided into four main tasks and subtasks as described below:

## 3.1 PHASE 1 TASKS AND PROJECTED ACCOMPLISHMENTS

### 3.1.1 Task 1 Information Required for the National Environment Policy Act

Minimal environmental documentation was needed for this project to comply with the National Environmental Policy Act because this sampling project will not disturb the existing environment, release any hazardous materials, or generate such materials. The project will not depend on access to classified areas, will not require construction of new buildings, and will be of short duration. No need for permits is anticipated. Space requirements will be minimal: probably one standard office for personnel and space for a trailer containing the test equipment.

The only potential sources of impact are those associated with contamination of the equipment used to withdraw samples from the exhaust streams of the ORNL incinerator. However, this contamination is not expected to be a source of significant environmental impact because decontamination of the equipment should be quite feasible. Even if that proves infeasible,

the volume of material (sensor, pipes, and/or pumps) that would be contaminated would be less than 2 cubic meters, and the consumption of landfill space therefore would be small.

No novel health and safety issues are anticipated. Standard methods will be appropriate to control the spread of contamination. We anticipate that all necessary details of the existing biologic, geologic, and socioeconomic aspects of the environment of ORNL will be available in prior NEPA documents for ORNL, ORNL health and safety records, and facilities plans. Detailed noise, cultural, archaeologic, and historic resource, land use, waste management, and socioeconomic data will not be needed. The data that will be required can be obtained from county planning and tax authorities.

### 3.1.2 Task 2 Laboratory Instrument Development

A laboratory prototype instrument for gaseous and particulate chemical analysis and monitoring will be designed and its subsystems constructed. The instrument will use an existing ion trap detector (ITD) mass spectrometer. A sampler will be designed, constructed, and tested as the front-end to the mass spectrometer. This sampler will serve to separate vapors from particulates so that both can be analyzed in optimum fashion. The particulate sampler will employ a commercial optical particle detector (which uses laser light scattering) as a trigger for pulsed electron-impact ionization. Particulates will be vaporized on the surface of a heated filament. Volatile organic compounds and other volatile compounds will be sampled by a dimethylsilicone membrane with an alternative direct vapor inlet. The ITD will be configured with a volcano-style field ionization source and its general operational characteristics verified.

**Task 2.1 Sampler Development** This subtask addresses the development of the real-time sampling component that consists of two major subunits, the vapor separator and the particulate sampler. The sampler is a critical element of the instrument, and its operational specifications will directly affect the development of both the vapor and particulate characterization instrumentation.

**Task 2.2 Vapor Characterization and Monitoring Instrumentation** This subtask involves several stages, including the integration of a microfabricated volcano field ionization (FI) source with an ion trap detector (ITD), verification of the operation of the FI-ITD for organic vapor analysis, and interfacing of the vapor sampler with the FI-ITD. The end product of this subtask will be an instrument capable of providing real-time characterization of organic vapors sampled directly from a process stream or stack.

**Task 2.3 Particulate Characterization and Monitoring Instrumentation** This subtask involves several stages, including the modification of an ITD for *in-situ* particulate pyrolysis (Py), verification of the operation of Py-ITD, interfacing of the particulate sampler with the Py-ITD. The end product of this subtask will be an instrument capable of providing real-time characterization of particulates sampled directly from a process stream or stack.

### 3.1.3 Task 3 Laboratory Testing

This laboratory system will then undergo extensive testing, with modifications as needed. The tests will include sensitivity, quantitation, and long-term stability analysis for both laboratory-produced organic vapors and particulates having micrometer and submicrometer dimensions. The vapors and particulates will consist of independently confirmed concentrations in air, particle sizes, and relative chemical abundances. The laboratory-produced vapors and particulates will initially be composed of single-component vapors or particulate chemistries (such as metal oxides), and testing will then progress to multiple-composition samples. We will search for any matrix effects in relative and absolute sensitivities for the multiple-composition samples.

**Task 3.1 Single Metal and Single Organic Vapor Test Atmosphere Testing** This testing subtask challenges the instrument with only a single organic vapor at a time to determine the level of detectability (LOD). A variety of representative vapors will be used to show the general range of LOD available using this technology. Corresponding tests will be conducted using particulates of varying sizes composed of single metal and inorganic species.

**Task 3.2 Multiple Metal and Multiple Organic Vapor Test Atmosphere Testing** This testing subtask challenges the instrument with multiple, mixed organic vapors to determine the level of detectability (LOD) of each species in a mixture. A variety of representative vapors were used to show the general range of LOD available using this technology. Corresponding tests have been conducted using particulates of varying sizes composed of multiple metal and inorganic species. Additional tests will be conducted using representative mixtures of organic vapors and particulates simultaneously to determine both LOD and matrix effects.

### 3.1.4 Task 4 Phase 2 Design Documentation

A subscale integrated system design document will be produced for a subscale integrated system for development in Phase 2.

## 3.2 PHASE 1 ACCOMPLISHMENTS

During the initial period of performance, the primary effort under Task 1 was directed toward providing the DOE with the requisite information relating to the NEPA documentation. In addition, a number of reports and project initiation documents were prepared in accordance with the requirements of the contract. Because no laboratory effort could be undertaken before completion and approval of the NEPA documentation, only a limited amount of effort was expended on the project, primarily in the form of more extensive literature surveys and project startup meetings within SRI.

On November 25, 1992, a letter from Randolph L. Kesling, Contracting Officer, Morgantown Energy Technology Center, verified that this project was granted a categorical exclusion for the Phase 1 effort under the DOE National Environmental Policy Act. A project startup meeting was therefore scheduled for December 15, 1992, at Morgantown.

At the project kickoff meeting, both Michael J. Coggiola, SRI's project leader, and Clyde Witham, leader of the sampler development task were present. DOE representatives included William Huber, the COTR from DOE/METC, Ronald Roth, DOE/METC contracts, and Al Tardiff from DOE headquarters. Additional DOE/METC technical personnel attended as well. Although a technical representative from ORNL was scheduled to attend, he was unable to do so.

William Huber began the meeting with introductions, followed by an overview of METC presented by Robert Bedick. Michael Coggiola then reviewed the technical aspects of the project, including background information, goals, and schedule. Ronald Roth reviewed the contractual details relating to the phased acquisition of this program. During the open discussion period, Al Tardiff from DOE headquarters described several parallel, related projects currently under way at other DOE facilities with which we would need to coordinate our efforts to avoid duplication. It was further agreed that a visit to the TSCA incinerator site at ORNL would be beneficial for both SRI and DOE representatives. No formal plans for this trip were made during the meeting. However, due to conflicts with the TSCA operating schedule, no visits were made during Phase 1 by either SRI or METC personnel.

The week following the kickoff meeting at METC, the principal task leaders met at SRI to allocate resources between the tasks (in the form of establishing project subaccounts) and to begin assigning and scheduling personnel. Work on Tasks 2.1, 2.2, and 2.3 began in early 1993.

The primary effort under Task 2.1 was devoted to initiating the design for a particulate sampler. Previously used particulate samplers were examined for their adaptability to this project, and details regarding the specific sampling conditions that will prevail at the ORNL test site were obtained. Although the exact sampling requirements (such as particle size, gas flows, temperatures, physical sizes and limitations,) are not as yet clearly defined, a preliminary sampler design has been started based on the most likely operating conditions. This design is also being integrated with the instrument design to ensure proper sample transport, to minimize losses, and to satisfy the mass spectrometer's vacuum and gas load restrictions. Because the sampler design is flexible with regard to gas flows, orifice sizes, and transport distances, modifications can easily be made as detailed conditions become available. In any case, it was likely that the Phase 1 sampler design would need to be modified slightly from the field prototype to accommodate the laboratory test facilities at SRI.

Development of the vapor instrument under Task 2.2 was actually broader in scope because it involved adapting the ion trap mass spectrometer to operate in a larger, more accessible vacuum system that could be used for both vapor and particulate testing. Using many existing vacuum components, including turbomolecular-pumped vacuum chambers and suitable vacuum feedthroughs for electrical and sample connections, we modified one of our laboratory ion trap detectors and installed it in the test chamber. Initially, the ion trap was tested using directly introduced vapor samples and conventional electron impact ionization to verify that it operated correctly in the new vacuum housing.

The first step in development of the particulate instrument under Task 2.3 was to design a vacuum system. Extensive calculations were made of the expected gas loads, pumping requirements, and resultant operating pressures. These detailed calculations include estimates of particle light scattering signal levels. Using available vacuum pumps and components to the extent possible and purchasing some commercially available specialty items such as the skimmer cones, we arrived at a workable design for the laboratory prototype system, shown schematically in Figure 1.

### 3.2.1 Vacuum System Pumping Calculations – Initial Design

The following assumptions were made concerning the operating conditions within the four vacuum regions of the instrument:

1. Inlet pressure = $P_I$ = 50 Torr (Region I).
2. Main chamber gas load of $\lesssim 10^{-6}$ Torr (requires 2 differential pumping stages).
3. Use available pumps:
   Region II: 5.6 l/s Leybold D16A trivac mechanical pump
   Region III: 170 l/s turbopump (effective speed w/particle shield ≃ 135 l/s).
   Region IV: 270 l/s turbopump (effective speed w/particle shield ≃ 220 l/s).
4. Orifice diameters:
   Nozzle ($A_{12}$) = 250 μm
   Skimmer ($A_{23}$) = 390 μm (commercially available skimmer)
   Skimmer ($A_{34}$) = 600 μm (1.5 times skimmer $A_{23}$ diameter)

Based on these assumptions, the operating pressure in each region can be calculated as shown below.

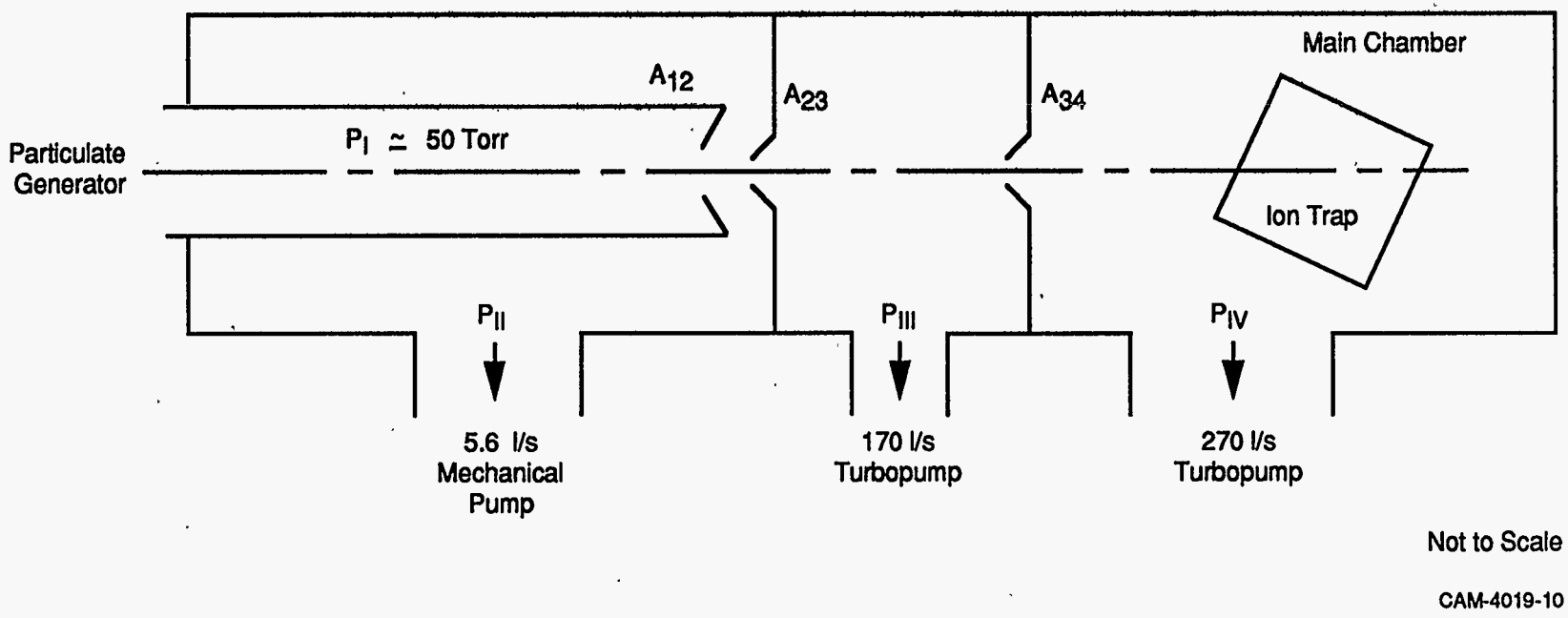


Figure 1. Schematic of the vacuum system defining the four pumping regions ($P_I$–$P_{IV}$ and the three beam-defining apertures ($A_{12}$–$A_{34}$).

**Region I** $P_I = 50$ Torr (assumed)

**Region II** Mass flow through $A_{12}$ $= \dot{m} = (14.3)(D_o)^2 P_I$, where $D_o = A_{12}$ diameter (cm)

$= 14.3\ (0.0250\ \text{cm})^2\ (50\ \text{Torr})$

$= 0.45$ Torr l/s

With a 5.6 l/s mechanical pump, the estimated pressure in Region II is

$$P_{II} = \frac{0.45\ \text{Torr l/s}}{5.6\ \text{l/s}} \simeq \boxed{0.080\ \text{Torr}}$$

**Region III** Distance between nozzle $A_{12}$ and skimmer $A_{23}$ is governed by the position of the Mach disk, assuming continuous free jet expansion. Skimmer $A_{23}$ should be placed in the zone of silence before the Mach disk.

Mach disk location $= X_M = (0.67)\left(\frac{P_o}{P_b}\right)^{\frac{1}{2}} (d)$ where d = nozzle diameter = 0.025 cm

$= (0.67)\left(\frac{50}{0.08}\right)^{\frac{1}{2}} (0.0250\ \text{cm})$ $P_o$ = nozzle stagnation pressure = $P_I$

$X_M = 0.42$ cm $P_b$ = background pressure = $P_{II}$

Based on the Mach disk calculation, skimmer $A_{23}$ should be placed $\lesssim$0.4 cm from nozzle $A_{12}$.

Mach disk reference: D. R. Miller in *Atomic and Molecular Beam Methods*, G. Scoles, Ed. (Oxford University Press, New York, 1988), p. 15.

Using this distance and the Region I pressure, we can calculate the number density at the skimmer location as follows:

Number density at skimmer $A_{23}$ $= n = (0.161)\ (3.24 \times 10^{16}\ \frac{\text{atoms}}{\text{cm}^3/\text{Torr}})\ (P_I) \left(\frac{A_{12}\ \text{nozzle diameter}}{A_{12}\ \text{to}\ A_{23}\ \text{distance}}\right)^2$

$= (0.161)\ (3.24 \times 10^{16}\ \frac{\text{atoms}}{\text{cm}^3/\text{Torr}})\ (50\ \text{Torr}) \left(\frac{0.025\ \text{cm}}{0.4\ \text{cm}}\right)^2$

$= 1.02 \times 10^{15}\ \text{atoms/cm}^3$

At a velocity of $v \simeq 4 \times 10^4$ cm/s, the flux at skimmer $A_{23} = nv$

$\simeq (4 \times 10^4\ \frac{\text{cm}}{\text{s}})\ (1.02 \times 10^{15}\ \frac{\text{atoms}}{\text{cm}^3}) \simeq 4.1 \times 10^{19}\ \text{atoms/cm}^2\cdot\text{s}$

The numbers of atoms passing through $A_{23}$ into Region III is given by

$$(4.1 \times 10^{19} \text{ atoms/cm}^2\text{·s}) \left(\frac{\pi}{4} \times (\text{diameter } A_{23})^2\right) = (4.1 \times 10^{19}) \left(\frac{\pi}{4}\right) (0.0390)^2$$
$$\simeq 5.2 \times 10^{16} \text{ atoms/s}$$

The gas load entering region III consists of two contributions, one associated with the molecular beam formed by the gas dynamic expansion through $A_{23}$, and the other arising from the normal gas diffusion from the higher ambient pressure in Region II.

The throughput contribution from the molecular beam ($Q_{III,MB}$) is given by

$$Q_{III,MB} = \frac{5.2 \times 10^{16} \text{ atoms/s}}{3.24 \times 10^{19} \text{ atoms/l·Torr}} \simeq 1.6 \times 10^{-3} \text{ Torr·l/s}$$

while the throughput associated with diffusion across $A_{23}$ ($Q_{III,D}$), is found from

$$Q_{III,D} = P_{II} \times \text{aperture } A_{23} \text{ conductance}$$
$$= (0.08 \text{ Torr}) (9.15) (0.0390 \text{ cm})^2 \simeq 1.2 \times 10^{-3} \text{ Torr·l/s}$$

The combined throughput in region III ($Q_{III} = Q_{III,MB} + Q_{III,D}$) $\simeq 2.8 \times 10^{-3}$ Torr l/s. Therefore, the estimated pressure in Region III is

$$P_{III} \simeq \frac{2.8 \times 10^{-3} \text{ Torr l/s}}{135 \text{ l/s}} \simeq \boxed{2.1 \times 10^{-5} \text{ Torr}}$$

**Region IV** The distance between the forward edges of skimmers $A_{23}$ and $A_{34}$ is assumed to be $\simeq 6.41$ cm to allow adequate space for light collection optics.

Skimmer $A_{23}$ forms a molecular beam source with a solid angle of

$$\text{Solid angle of skimmer } A_{23} \text{ (viewed from nozzle)} = \frac{\pi/4 \ (0.040 \text{ cm})^2}{(0.4 \text{ cm})^2} = 7.85 \times 10^{-3} \text{ steradians}$$

$$\text{The beam flux exiting skimmer } A_{23} = \frac{8.2 \times 10^{17} \text{ atoms/s}}{7.85 \times 10^{-3} \text{ steradians}} = 6.6 \times 10^{18} \text{ atoms/steradian·s}$$

The amount of gas reaching skimmer $A_{34}$ depends on its relative solid angle as

$$\text{Solid angle of skimmer } A_{34} \text{ (viewed from nozzle)} = \frac{\pi/4 \ (0.060 \text{ cm})^2}{(6.41 \text{ cm} + 0.4 \text{ cm})^2} \simeq 6.1 \times 10^{-5} \text{ steradians}$$

The flux through skimmer $A_{34}$ = ($6.6 \times 10^{18}$ atoms/s steradian) ($6.1 \times 10^{-5}$ steradians)

$$= 4.0 \times 10^{14} \text{ atoms/s} = Q_{IV,MB}$$

Assuming a gas velocity v = $4 \times 10^4$ cm/s, the number density at skimmer $A_{34}$ is found as

$$= \frac{4.0 \times 10^{14} \text{ atoms/s}}{(4 \times 10^4 \text{ cm/s})\ (2.8 \times 10^{-3} \text{ cm}^2)}$$
$$= 3.6 \times 10^{12} \text{ atoms/cm}^3$$

This number density corresponds to a pressure of ~0.11 Torr at 300 K. The gas load entering region IV also consists of two contributions, one associated with the molecular beam formed by the gas dynamic expansion through $A_{34}(Q_{IV,MB})$ and the other arising from the normal gas diffusion ($Q_{IV,D}$) from the higher ambient pressure in Region III.

The throughput contribution due to the molecular beam is

$$Q_{IV,MB} = \frac{4.0 \times 10^{14} \text{ atoms}}{3.24 \times 10^{19} \text{ atoms/l Torr}} \simeq 1.2 \times 10^{-5} \text{ Torr l/s}$$

while the corresponding throughput associated with the diffusion across $A_{34}$ is

$$Q_{IV,D} = (2.1 \times 10^{-5} \text{ Torr}) (9.15) (0.06 \text{ cm})^2$$
$$\simeq 6.9 \times 10^{-7} \text{ Torr l/s}$$

Combining throughputs $Q_{IV,MB}$ and $Q_{IV,D}$ gives

$$Q_{IV} \simeq 1.3 \times 10^{-5} \text{ Torr l/s}$$

Therefore, the estimated pressure in Region IV is

$$P_{IV} \simeq \frac{1.3 \times 10^{-5} \text{ Torr l/s}}{220 \text{ l/s}} \simeq \boxed{5.9 \times 10^{-8} \text{ Torr}}$$

### 3.2.2 Collection of Scattered Laser Light

The following parameters were determined for collection of scattered laser light.

Thin lens formula: $\frac{1}{s_o} + \frac{1}{s_i} = \frac{1}{f}$ where $s_o$ = object distance

$s_i$ = image distance = location of photomultiplier tube (PMT)

$f$ = lens focal length

Magnification: $M = \frac{s_i}{s_o}$

Collection solid angle: $\Delta\Omega = \frac{\pi}{4} \times \frac{(\text{clear aperture diameter})^2}{s_o^2}$

Constraints:

1. Lens and mounting tube must fit through a 3.5-cm-diameter tube on the vacuum housing.
2. Desire that $s_i \geq 12$ cm so that the image is focused outside of the chamber at the focal plane the PMT.
3. Use standard stock commercial lenses.

For a standard 3.25-cm-diameter aspheric condenser lens with an effective focal length of 2.35 cm (thickness: 1.35 cm), Table 1 lists the calculated optical parameters.

**Table 1. Light Scattering Parameters**

| Object Distance, $s_o$ (cm) | Image Distance, $s_i$ (cm) | Magnification M | Collection Solid Angle, $\Delta\Omega$ |
|---|---|---|---|
| 2.92 | 12.0 | 4.1 | 0.74 |
| 2.79 | 15.0 | 5.4 | 0.82 |
| 2.66 | 20.0 | 7.5 | 0.92 |

Given the dimensions and constraints imposed by the vacuum housing, an image distance of 15 cm is optimum, resulting in a collection solid angle of 0.82 steradians. The number of photons per steradian that would be scattered by a particle of a given size (assumed to be either 0.2 or 0.5 μm) is calculated as follows. Assume a 4-mW HeNe laser focused to a 0.1-cm-diameter spot size and a particle velocity of $4 \times 10^4$ cm/s. The number of scattered photons, $N_{ph}$, is given by

$$N_{ph} = I_L \left(\frac{d\sigma}{d\Omega}\right)(d\Omega)t$$

where $I_L$ = intensity of laser light

$t$ = time

$\frac{d\sigma}{d\Omega}$ = differential scattering cross section

The differential cross section for light scattering is calculated as

$$\frac{d\sigma}{d\Omega} = \frac{2\pi a^2}{4\pi} = \frac{1}{2}a^2$$

where $a$ = particle radius

The time element is associated with particle transit:

$$t = \frac{10^{-3}\ \text{m}}{4 \times 10^{2}\ \text{cm/s}} = 2.5 \times 10^{-6}\ \text{s}$$

For a 0.2-μm particle,

$$a = 0.1 \times 10^{-4}\ \text{cm and} \frac{d\sigma}{d\Omega} = 5 \times 10^{-11}\ \text{cm}^2/\text{sr}$$

hence,

$$N_{ph} = \frac{4 \times 10^{-3}\ \text{J/s}}{10^{-2}\ \text{cm}^2} \times 5 \times 10^{-11} \frac{\text{cm}^2}{\text{sr}} \times d\Omega \times 2.5 \times 10^{-6}\ \text{s} \times \frac{1\ \text{eV}}{1.6 \times 10^{-19}\ \text{J/eV}} \times \frac{1\ \text{photon}}{2\ \text{eV}}$$

$$= 156\ \text{photons/sr} \times d\Omega$$

In a solid angle of 0.82 sr (see above) for the collection lens,

$$N_{ph}\ \text{collected} \simeq (0.82\ \text{sr})\ (156\ \text{photons/sr}) \simeq \boxed{128\ \text{photons}}$$

For a 0.5-μm particle,

$$a = 0.25 \times 10^{-4}\ \text{cm and} \frac{d\sigma}{d\Omega} = 3.1 \times 10^{-10}\ \text{cm}^2/\text{sr}$$

$$N_{ph} = 966\ \text{photons/sr} \times d\Omega$$

In the solid angle of 0.82 sr,

$$N_{ph}\ \text{collected} \simeq \boxed{792\ \text{photons}}$$

Given the typical quantum efficiency and dark count of photomultiplier tubes in the HeNe wavelength region, the number of *detected* photons is above background. Changes in the optics and additional calculations may be needed, however, to increase the light scattering intensities to allow for uniformity in the light scattering cross section, optics losses, and high levels of scattered background light.

The vacuum test chamber that was constructed based on these calculations is shown in Figure 2. The photograph shown in Figure 2 was taken after the initial vacuum system design was modified by the addition of a diffusion pump in Region II (see below). The particle generation system (not visible in the photograph) is located to the left of the vacuum system. The three differentially pumped regions are readily apparent, as are the two photomultiplier housings mounted on each side of the beam line. The original ITD chassis is visible to the rear of the apparatus, with the high voltage rf line exiting through the opening normally used for the GC inlet transfer line.

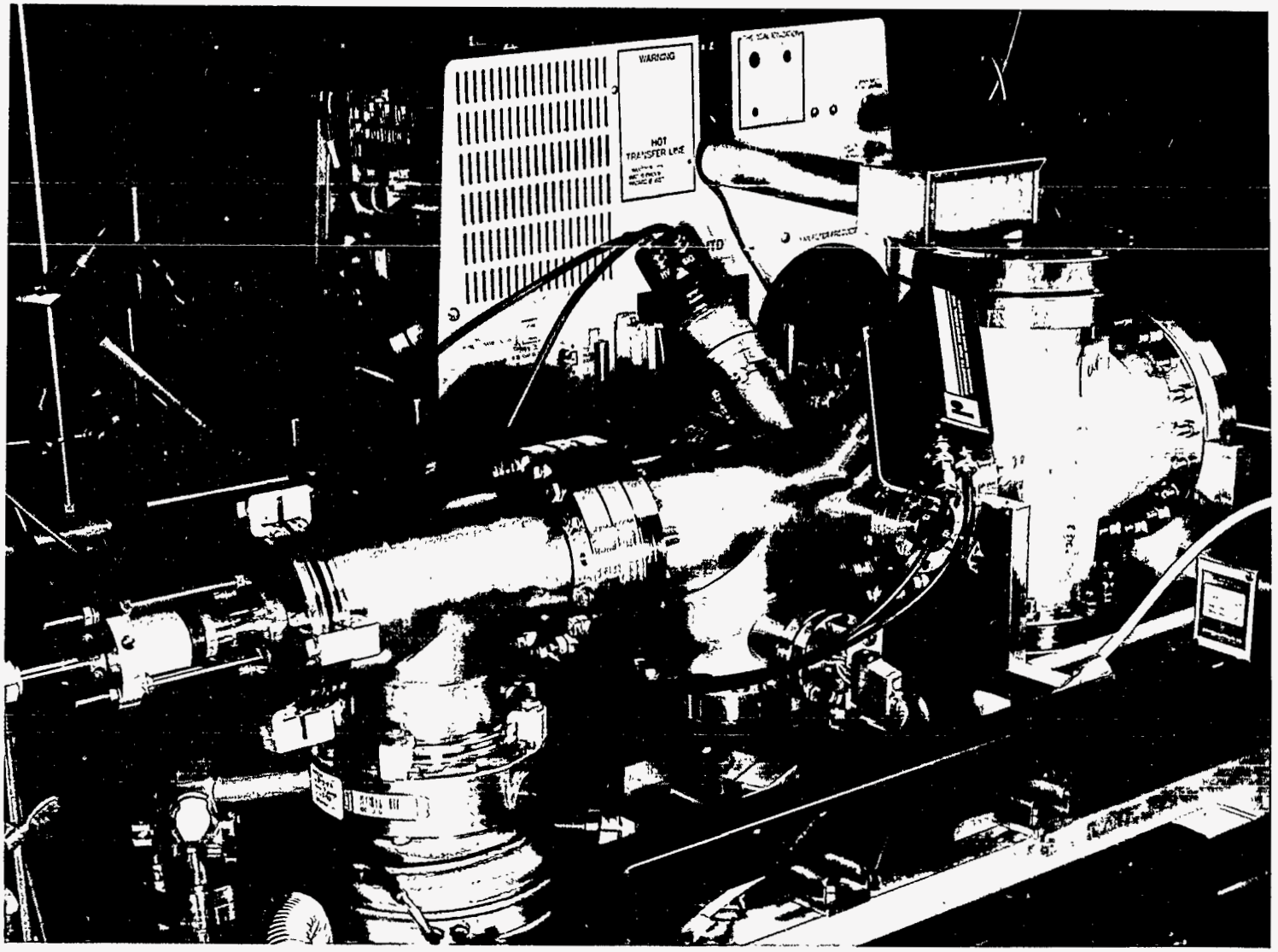


CP-4019-11

Figure 2. Photograph of the laboratory prototype system.

### 3.2.3 Inlet Design Considerations

The design of the inlet to the mass spectrometer depends on the particulate concentration anticipated in the stack sample and on the sample processing rate of the ion trap. The air flowrate into the mass spectrometer will also determine the characteristics of the isokinetic sampling probe in the stack of the incinerator.

We received some information from Dr. William Bostick at ORNL regarding emissions from the K-1425 TSCA Incinerator. This information included total particulate levels, total hydrocarbons, some heavy metal emissions from the kiln, and some information on heavy metals in the stack after the ionizing wet scrubber. Table 2 summarizes this information. From this information, we estimate that the total particulate emission rate from the stack is about 0.2 mg/l (0.18 mg/l is the regulatory maximum for total particulate). The measured geometric mean diameter of the particulate in the stack is 1.14 μm with a standard deviation of 1.73. Since the size distribution is apparently log-normal, this allows us to compute a mass median diameter of about 4.82 μm and a number concentration (based on mass concentration and log-normal distribution) of approximately 6600 particles/$cm^3$.

The design sample rate of the mass spectrometer is 6 $cm^3$/min, and the ion trap can respond to a maximum of 20 events/s. The mass limitation of the ion trap is about 1 ng/s. Based on the estimates of particle concentration above, the stack sample would need to be diluted a minimum of 1:33 to meet the constraints of the ion trap, assuming no losses in transmission of the particles from the nozzle inlet through the system to the pyrolysis filament and no vapor losses after pyrolysis. A more realistic minimum is 1:100 dilution.

The EPA method 5 particulate sampling train samples at a minimum of 0.014 $m^3$/min. By using a sample probe as small as 0.32 cm diameter, we should be able to achieve isokinetic sampling at a sample rate as low as 3 l/min. This means that the stack sample will require splitting to achieve a representative sample of 6 $cm^3$/min for introduction into the mass spectrometer. The inlet sample splitter/dilutor is thus envisioned to have a fairly complex design allowing for variable dilution (probably by a factor of 100 to 1000) and for splitting off a sample at a ratio of about 1:2000.

### 3.2.4 Pyrolysis Filament Design

A major effort under Task 2.3 was to design, modify, and test another ion trap detector to operate with an internal pyrolysis filament for particulate analysis. It was planned that ultimately this second ion trap would be installed in the same vacuum chamber as the vapor instrument described above and share the same electronics and computer system. During this Phase 1 project, the two ion traps did not operate simultaneously, so vapor and particulate tests were done separately rather than concurrently. We initiated a design study for the heated pyrolysis filament to determine its optimum size, shape, material, and most critically, its placement within the ion trap volume. As a first step, we fabricated a simple filament loop from 0.013-cm-diameter Chromel wire and inserted it into one of the existing 0.11-cm-diameter holes in the exit end cap of the standard ITD. This arrangement allowed us to investigate not only the effects of thermal pyrolysis of materials preloaded onto the filament, but also the electrical behavior of the ion trap with this perturbation present.

Our first tests involved placing small amounts of either cadmium or zinc on the wire loop, then slowly heating the wire while recording mass spectra. Figure 3 shows a typical total ion current (TIC) for powdered cadmium recorded as a function of time (and therefore as a function of temperature since the filament was heated linearly with time). The single sharp peak at about 2 minutes is due entirely to the volatilization of cadmium from the filament.

**Table 2. TSCA Incinerator Data**

| Species | Kiln | Ref | Stack | Ref |
|---|---|---|---|---|
| | Mass Concentration | | | |
| | | | | Calculated assuming 90% removal |
| Total particulates | 2.0 mg/l | Various | 0.2 mg/l | |
| Total HCs | 100 ppm (vol) | " | | |
| Heavy metals | | | < 2 mg/l | (1% of total, Bostick) |
| Arsenic | | | < 340 ng/l | Shor et al. |
| Barium | | | 11.8 ng/l | " |
| Beryllium | | | 0.03 ng/l | " |
| Cadmium | | | 0.25 ng/l | " |
| Chromium | | | 20 ng/l | " |
| Copper | | | 8.4 ng/l | " |
| Lead | | | 33.3 ng/l | " |
| Magnesium | | | 57.5 ng/l | " |
| Manganese | | | 6.4 ng/l | " |
| Mercury | | | < 7.6 ng/l | " |
| Nickel | | | 4.8 ng/l | " |
| Phosphorus | | | 379 ng/l | " |
| Selenium | | | < 342 ng/l | " |
| Silver | | | 18.0 ng/l | " |
| Thallium | | | < 20.6 ng/l | " |
| Uranium | | | 20.2 ng/l | " |
| $UO_2$ | 1.5 µg/l | various | Since the scrubber efficiency is not | |
| $UO_2Cl_2$ | 0.75 µg/l | " | known, the stack levels for these | |
| BeO | 0.15 µg/l | " | species cannot be estimated at | |
| PbO | 3.0 µg/l | " | the present time. | |
| $PbCl_2$ | 0.3 µg/l | " | | |
| | | Size Distribution | | |
| Geometric mean diameter (µm) | | | 1.14 | Shor et al. |
| $U_g$ (µm) | | | 1.73 | " |
| Mass mean diameter (µm) | | | 4.82 | C. Witham calculation |

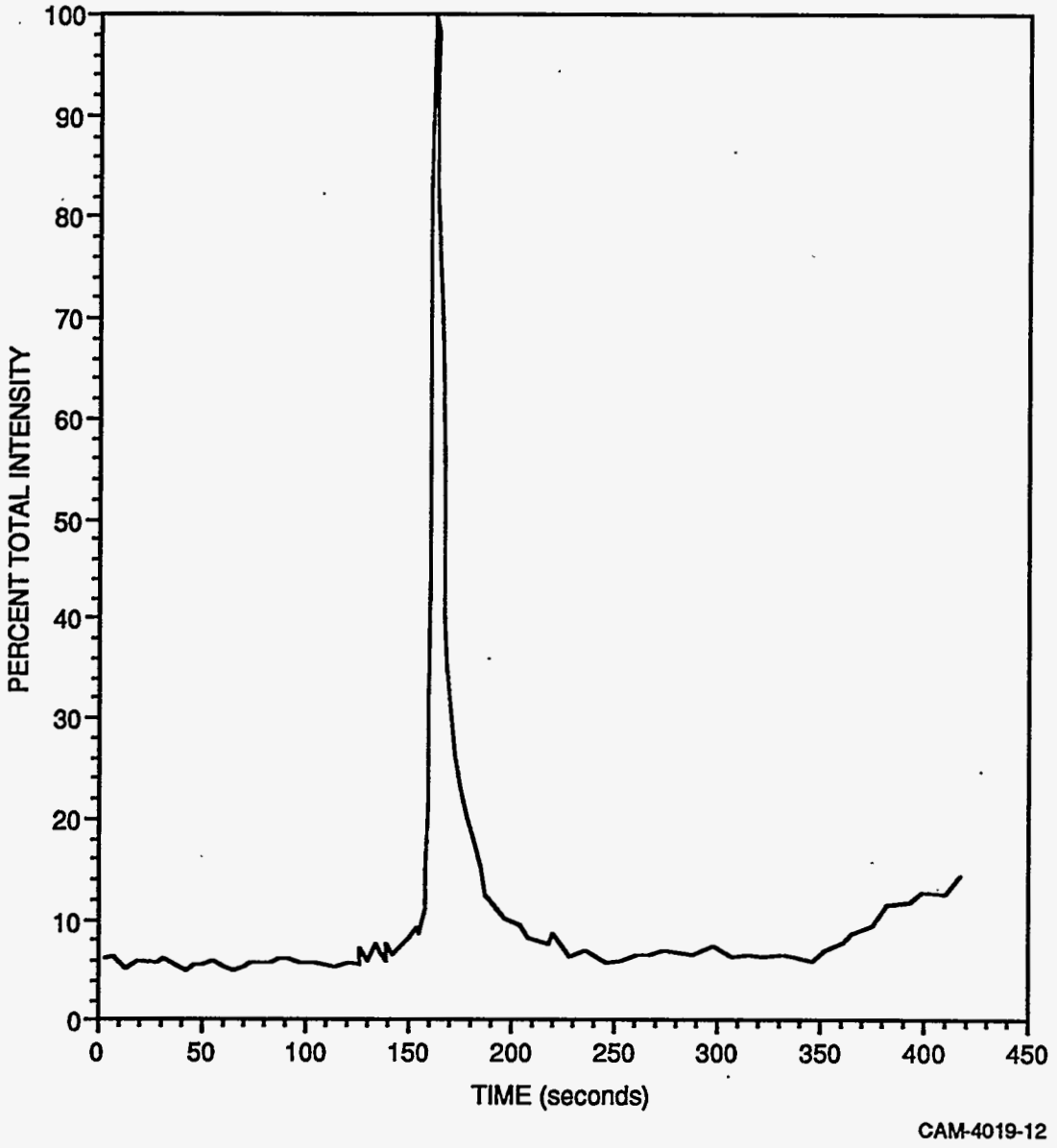


Figure 3. Total ion chromatogram for the volatilization of powdered cadmium from a filament within the ion trap.

Examination of the mass spectra recorded during this vapor evolution (Figure 4) clearly shows that all eight cadmium isotopes were readily detected. Moreover, the isotopic ratios listed in Table 3 agree reasonably well with the standard values. Similar results were obtained for zinc, as shown in Figures 5 and 6 and Table 4.

**Table 3. Comparison of Measured and Standard Isotopic Abundances for Cadmium**

| Mass | Measured | Standard |
|---|---|---|
| 106 | 0.52 | 1.25 |
| 108 | 0.52 | 0.89 |
| 110 | 12.3 | 12.49 |
| 111 | 13.0 | 12.8 |
| 112 | 25.2 | 24.13 |
| 113 | 12.6 | 12.22 |
| 114 | 28.6 | 28.73 |
| 116 | 7.22 | 7.49 |

**Table 4. Comparison of Measured and Standard Isotopic Abundances for Zinc**

| Mass | Measured | Standard |
|---|---|---|
| 64 | 48.4 | 48.63 |
| 66 | 28.0 | 27.9 |
| 67 | 4.9 | 4.1 |
| 68 | 18.7 | 18.75 |

While the use of simple wire loop is useful to establish some characteristics, the actual filament must be significantly larger to intercept the beam of particulates from the sampler. It must also be designed such that particles do not simply bounce off of the filament without being pyrolyzed. Our initial design focused on a Wood's horn shape fabricated from tantalum foil. This filament was tested to determine its heating and cooling characteristics and its particle collection/accommodation properties.

Pyrolysis filament designs were tested by using an optical pyrometer. We determined that the tantalum Wood's horn filament could be heated to 1800 using 30 A of current (see Table 5). Pyrolysis tests involved loading the filament with a small amount (a few μl) of latex beads suspended in water. As the filament was heated in 1-A increments, mass spectra were taken of any pyrolyzate produced. The appearance of pyrolysis products could then be correlated with the heater current and temperature. When the latex beads were used, clear evidence of pyrolysis was seen at very low heater currents (6 A). A representative mass spectrum is shown in Figure 7. Numerous peaks due to styrene and its fragments are apparent. At that current level, the filament temperature is too low to determine using the optical pyrometer, but was estimated at less than 600°C.

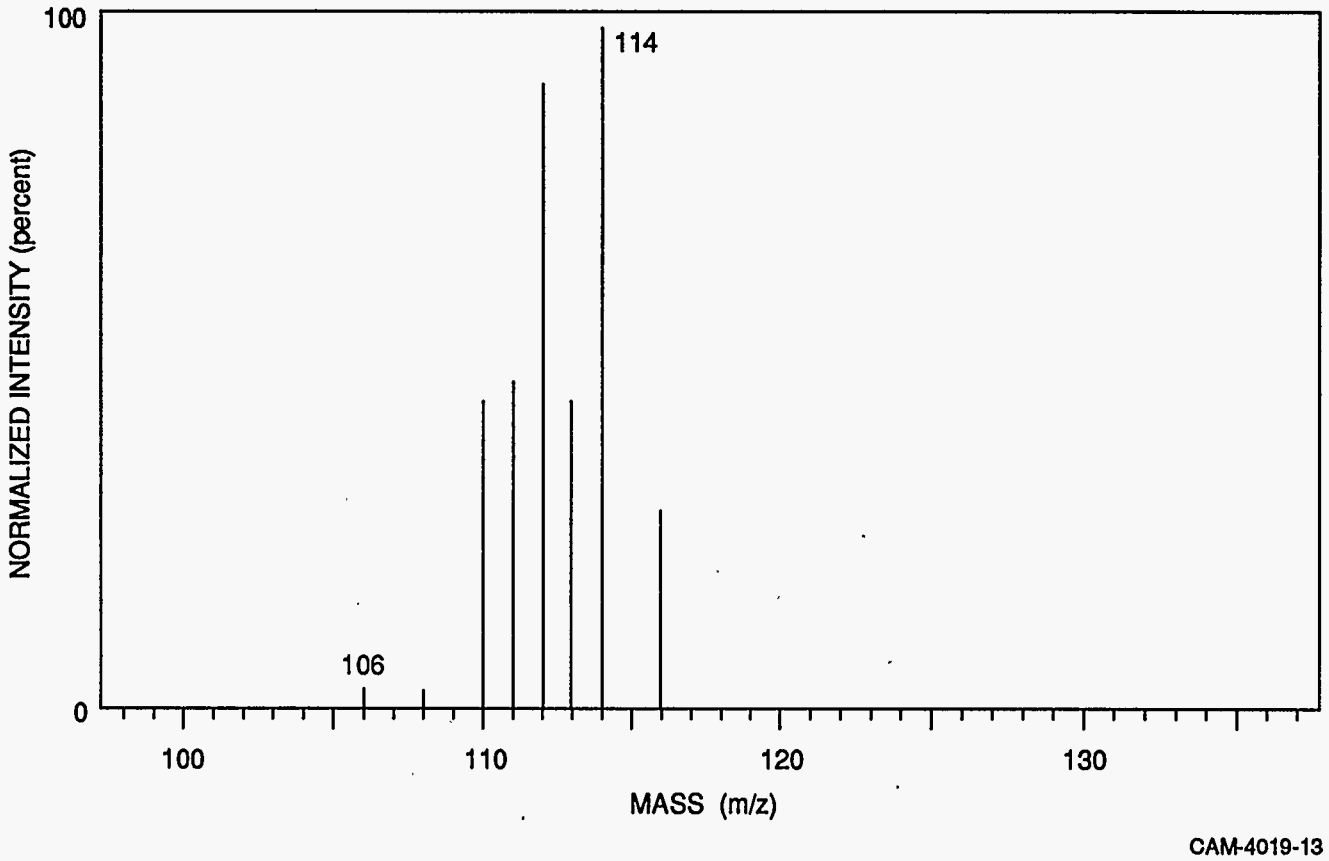


Figure 4. Mass spectrum recorded during the volatilization of powdered cadmium showing the measured isotopic distribution.

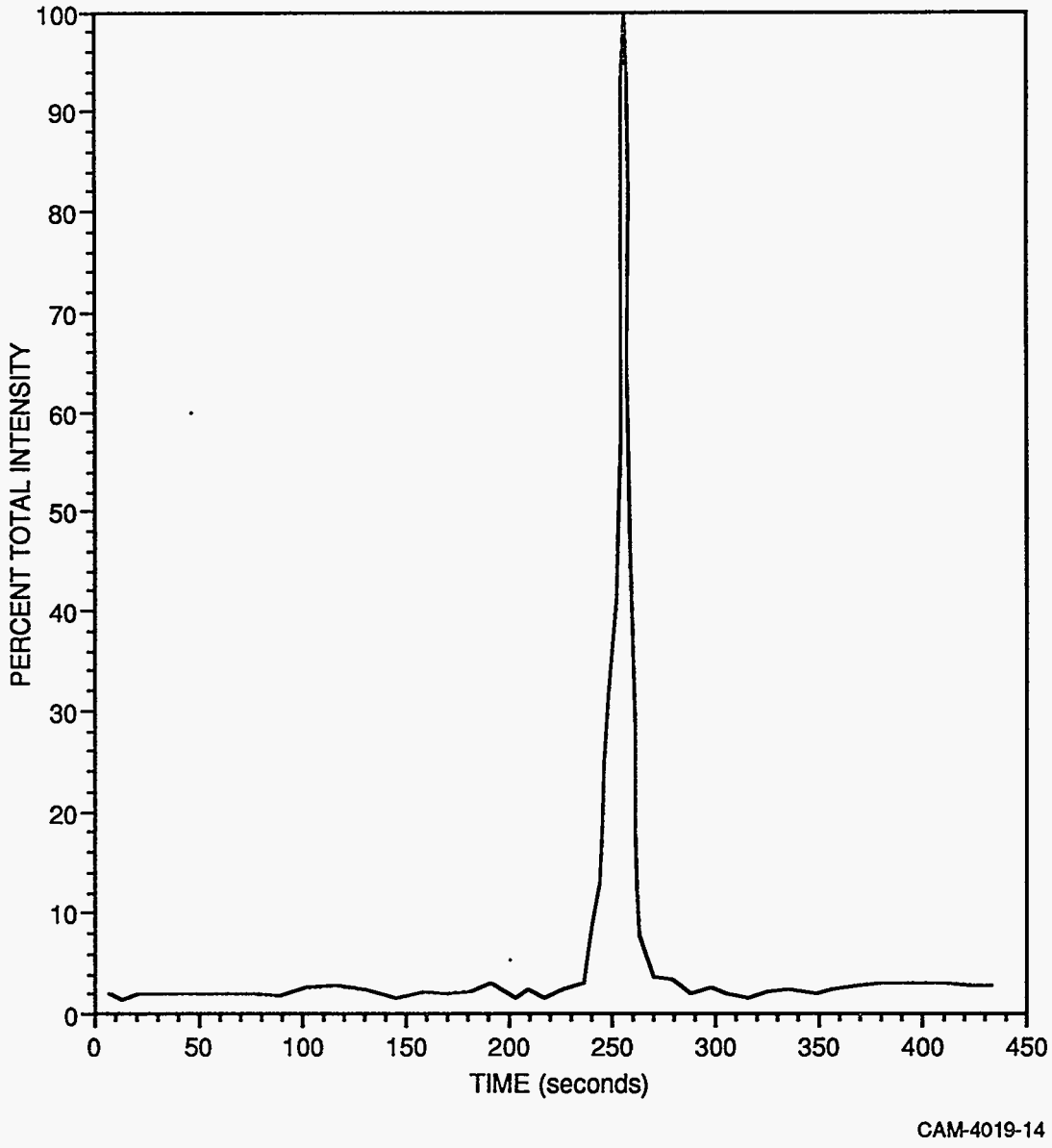


Figure 5. Total ion chromatogram for the volatization of powdered zinc from a filament within the ion trap.

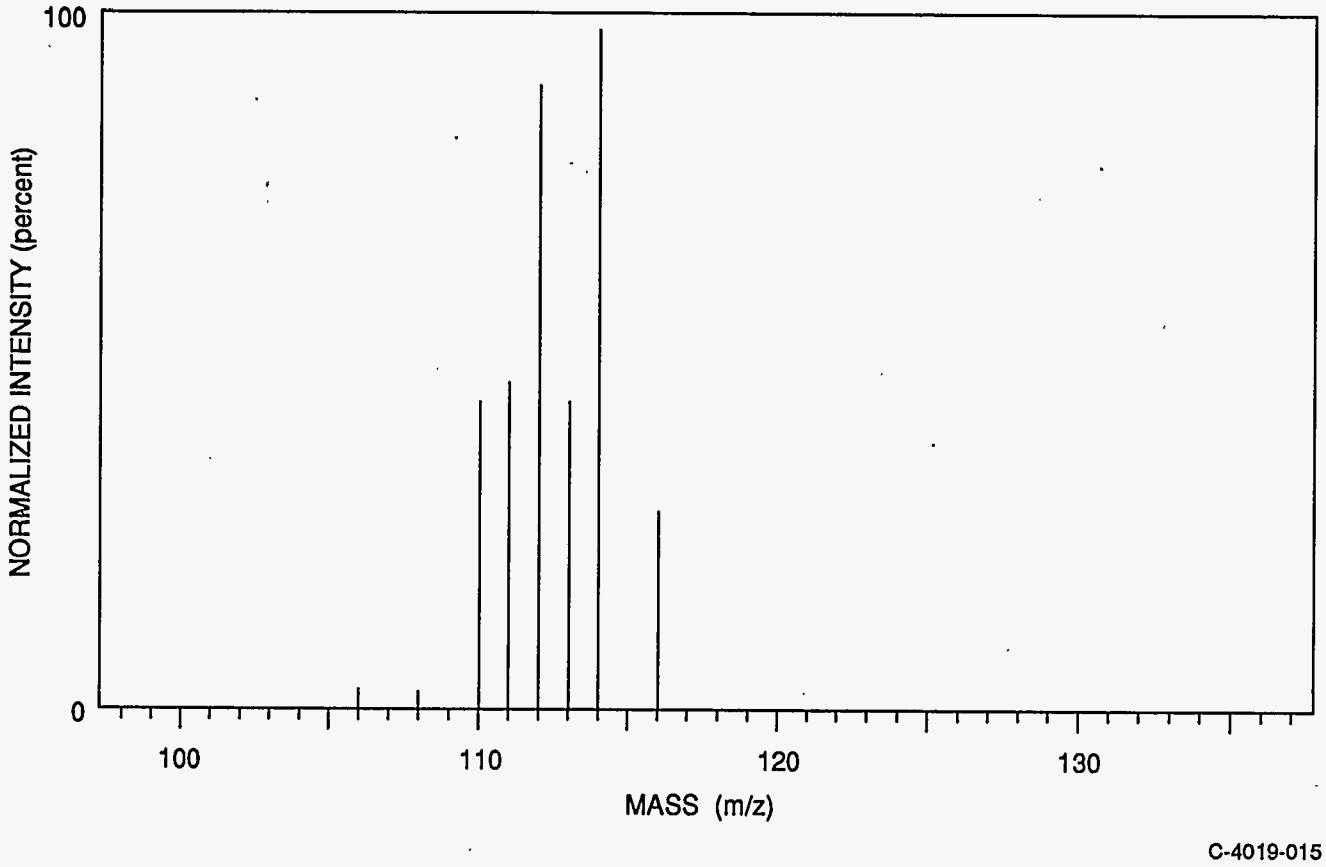


Figure 6. Mass spectrum recorded during the volatilization of the powdered zinc showing the measured isotopic distribution.

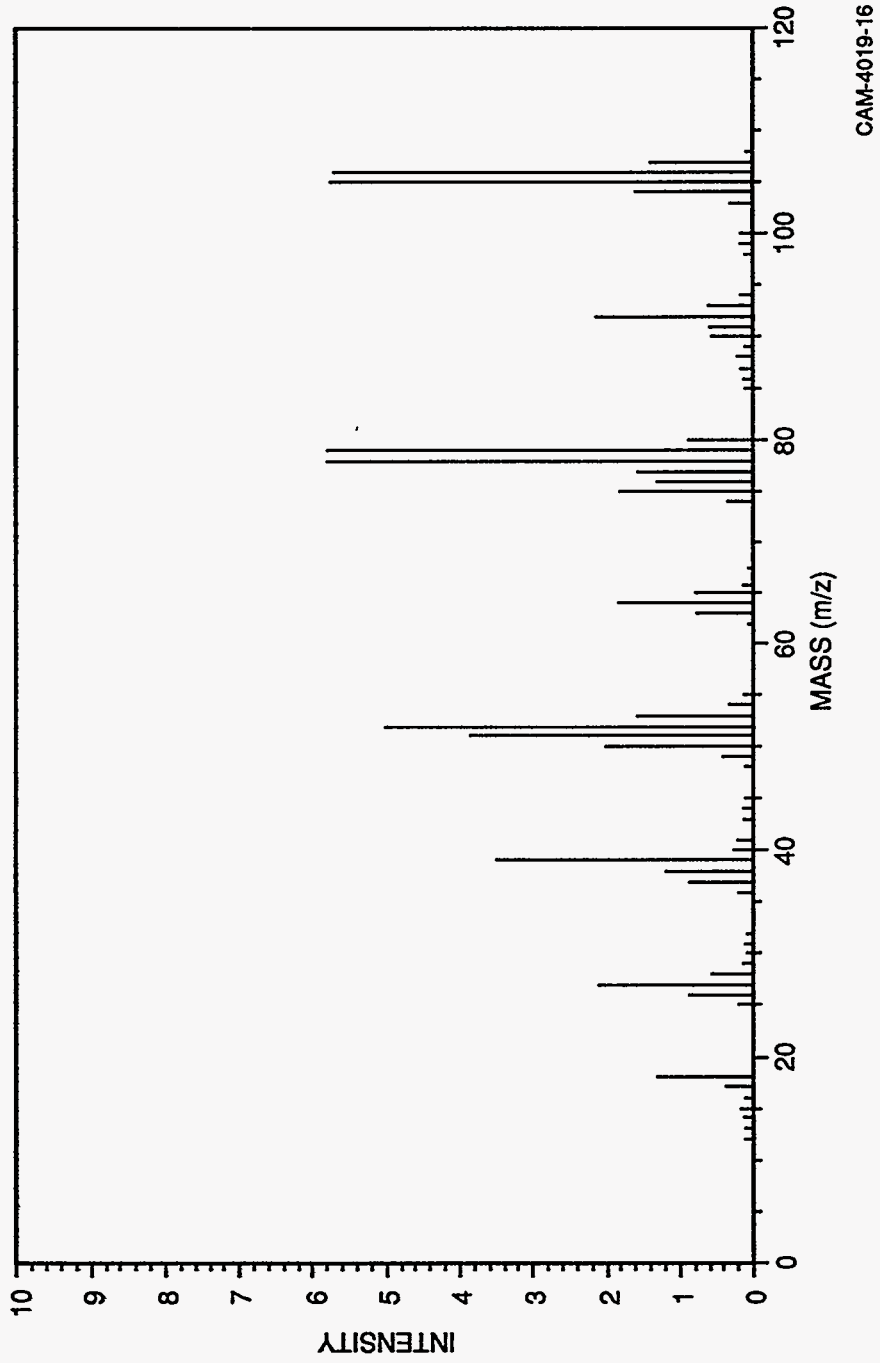


Figure 7. Mass spectrum of vapors emitted when latex particles are heated on a tantalum filament using 6 A of current.

**Table 5. Measured Temperature of Tantalum Pyrolysis Filament as a Function of Heater Current**

| Heating Current (A) | Temperature from Optical Pyrometer |
|---|---|
| 10 | 925 |
| 15 | 1150 |
| 20 | 1350 |
| 25 | 1575 |
| 30 | 1825 |

Subsequent experiments using samples of silver nitrate and silica, which required higher temperatures, showed similar results. Figure 8 shows the mass spectra recorded when approximately $3 \times 10^{-9}$ mol of silver (from $AgNO_3$) was placed on a tantalum filament and heated with 10 A of current. This heating current was previously determined to correspond to a temperature of about 925°C, as shown in Table 5.

Figures 9 and 10 compare the mass spectra recorded with $SiO_2$ loaded onto the filament at 0 and 30 A, respectively. Although the mass assignment for m/z 28 is somewhat ambiguous due to the interference from atmospheric $N_2^+$ and $CO^+$, comparison with a clean filament heated to the same temperature indicates that the majority of the m/z 28 signal is due to silicon ion fragments produced from vaporized $SiO_2$.

The final design for the filament is dictated by three factors: (1) required temperature range and heating rate, (2) particle capture efficiency, and (3) physical and electrical compatibility with the ion trap. Assessment of the third factor required a combination of computer modeling and actual experimentation with a working ion trap. We performed some computer simulations of the effect that various sized holes in the end caps have on the trapping fields of the ion trap mass spectrometer. The SIMION calculations indicated that little or no field distortion would result from a 0.3-0.4-cm-diameter hole placed near the ion exit in the end cap electrode. Since our preliminary design placed the hole in that location, it necessitated moving and shielding the electron multiplier that normally mounts just below the ion exit port. We then made some baseline sensitivity measurements with the ion trap in its normal configuration using both xenon and FC-43 (perfluorotributylamine). Following installation of an electrostatic shield between the electron multiplier and the eventual location of the pyrolysis filament, we repeated the sensitivity measurements and found that moving the multiplier had no measurable effect on the operation of the ion trap.

Before the optimum final diameter for the particle beam entrance channel was known, the position of the channel could be established based on the physical constraints of the ion trap geometry. We also determined that the most accurate method of drilling through both end caps is to (1) disassemble the trap, (2) drill through one end cap, (3) reassemble the trap, (4) use a pilot drill through the first hole to located the second hole, (5) disassemble the trap, and (6) drill the second hole. Using this approach, we drilled a 0.2-cm -diameter entrance channel through the ion trap at an 11° angle through the top electrode such that the particle will cross the center of the trap before exiting just to the side of the ion exit apertures. The entrance hole can be seen in Figure 11a just to the left of the filament assembly that is mounted in the center of the ion trap end cap

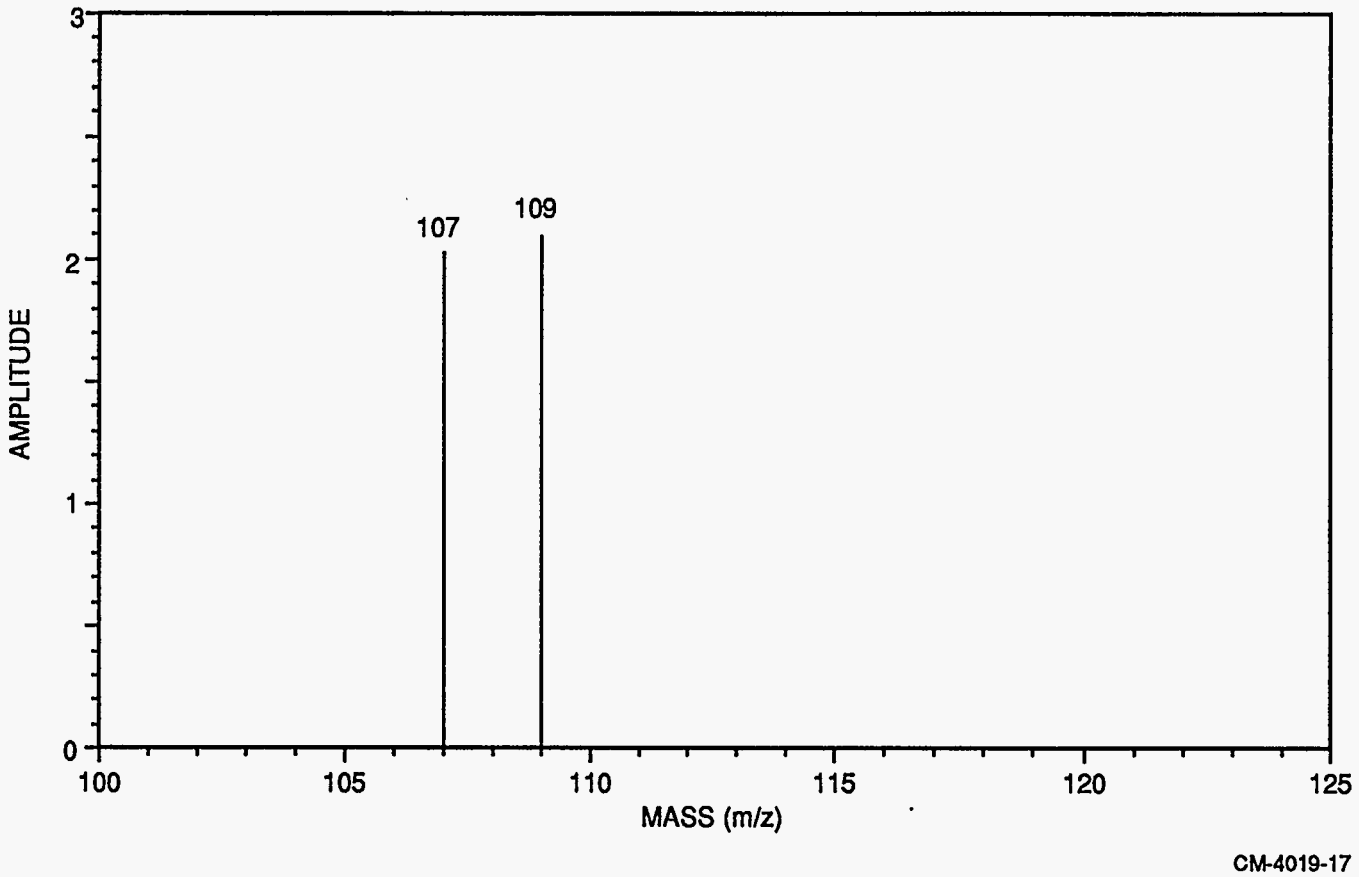


Figure 8. Mass spectrum of vapors emitted when 3 nM of silver nitrate is heated on a tantalum filament using 10 A of current.

The approximate filament temperature is 925 °C.

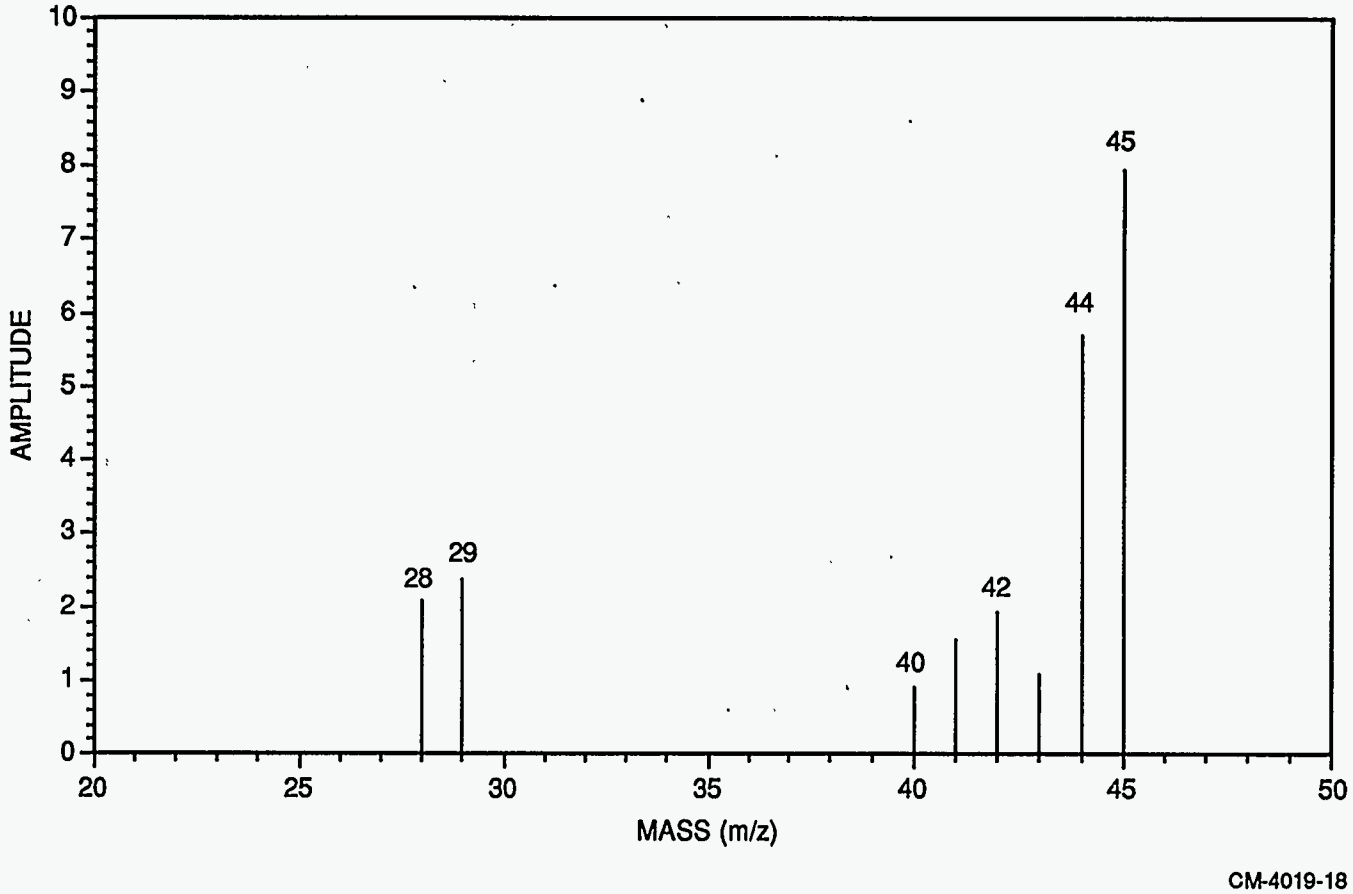


Figure 9. Mass spectrum of background recorded with an unheated tantalum filament loaded with 10 nm of $SiO_2$.

The approximate filament temperature is 1900°C.

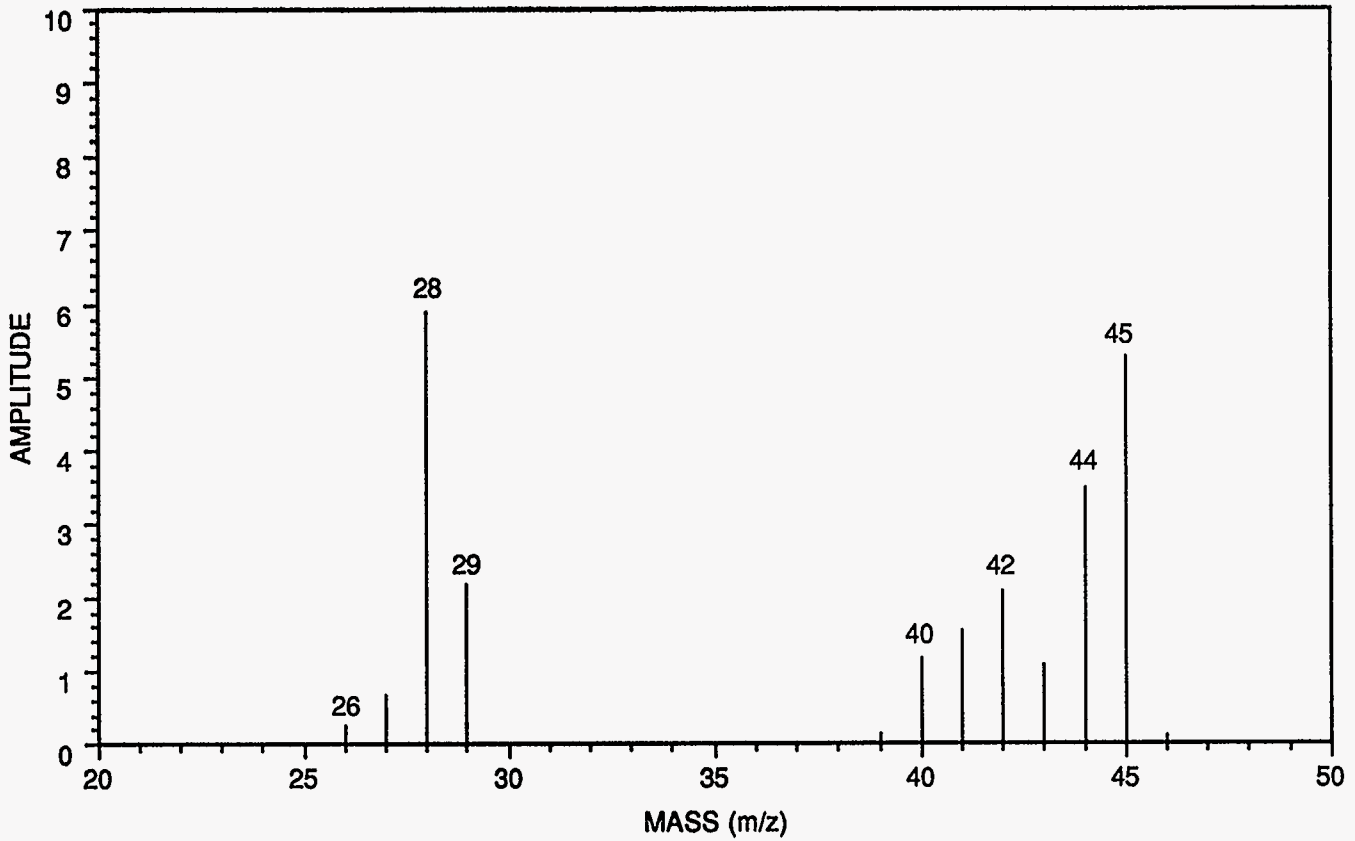


Figure 10. Mass spectrum of vapors emitted when 10 nm of $SiO_2$ is heated on a tantalum filament using 30 A of current.

The approximate filament temperature is 1900 °C.

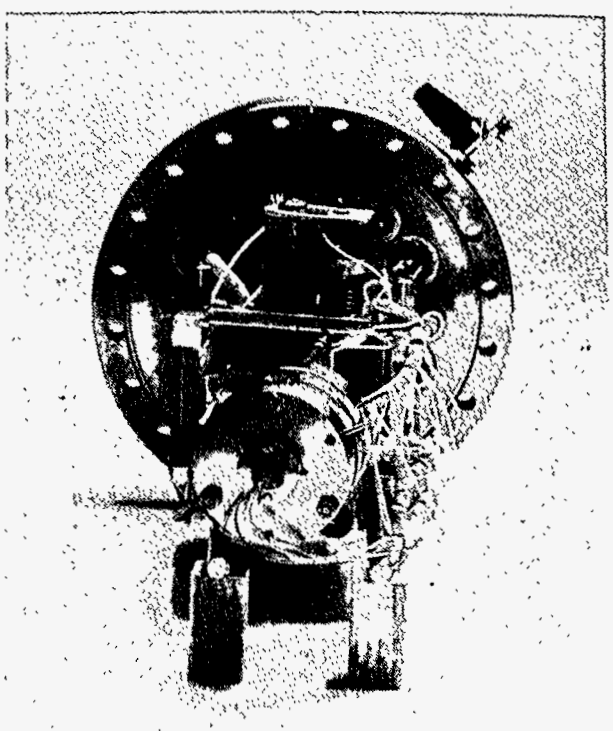

(a) End view showing the entrance hole just to the left of the filament assembly that is mounted in the center of the ion trap end cap.

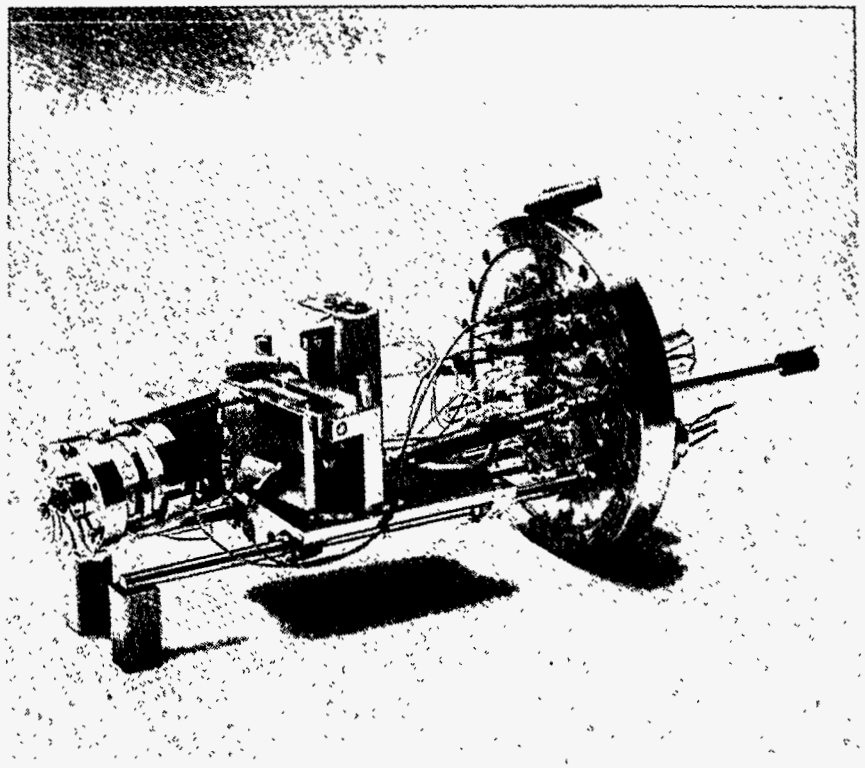

(b) Side view showing the three-axis alignment mechanism and the vacuum mounting flange.

CP-4019-20

Figure 11. Design of particulate ion trap.

To our knowledge, no one had previously drilled holes of this size or location in both end caps of anion trap. However, repeating the FC-43 and xenon measurements made earlier, we found no significant degradation in performance as a result of this channel.

Based on our estimate of the particle beam size, we drilled a 0.2-cm-diameter entrance channel through the ion trap mass spectrometer electrodes and found that there was no discernable loss in performance. We then fabricated a Macor support and a tantalum pyrolysis filament and mounted this unit onto the ion trap. While observing the normal background mass spectrum produced by the trap, we also observed that power to the pyrolysis filament was slowly increased. No changes in the background spectra were noted until the filament began to glow a dull red. At that point, the baseline of the mass spectra rose sharply, indicating the presence of many more ions that were not mass resolved. The most obvious source of these ions is electron impact ionization within the ion trap volume induced by the copious number of electrons generated by the hot filament. Since the electrons are emitted from the hot filament continually and are not synchronous with the mass scan, the ions appear to be unresolved and lead to a baseline increase. By application of a bias of +250 V dc to the filament, the thermal electron emission is suppressed, and the no baseline increase is seen until the filament reaches an approximate temperature of 1000-1100°C. At the higher power (15-16 A) required to reach this temperature, the areas surrounding the pyrolysis filament are heated, resulting in outgassing of adsorbed water vapor and other species. An improved electrostatic shield separating the filament from the electron multiplier was added.

Considerable progress was also made in overcoming the background problems observed when the pyrolysis filament was heated above 1000-1100°C. Several sources of outgassing were identified and corrected, and improved electrostatic and thermal shielding was installed between the filament and the detector. With these improvements, we can now apply 20-24 A to the pyrolysis filament for periods of 20-30 minutes with only slight increases in the background signal level. Using thermocouples on surrounding surfaces, we have found that most of the nearby ion trap components do not heat above 200°C under these conditions. Since all sources of outgassing have been removed other than normal water desorption, the most reasonable sources for the remaining background signal are thermal ions generated directly on the hot filament. We can eliminate this potential background source through appropriate electrostatic shielding at the entrance to the electron multiplier.

Because of both space constraints and safety considerations, the entire ion trap apparatus was moved to a different location during the project. As part of the move, we also enclosed the particle generation region and provided adequate ducting for the vacuum pump exhaust. These precautions were necessary so that when we begin testing with metal oxides, there will be no emission of respirable particles into the laboratory. We had anticipated that during the move, we would modify the vacuum chamber by adding the ion trap mounting platform in preparation for its installation. However, based on the difficulties that we encountered in aligning the particle beam delivery system with the differential pumping skimmers, was decided that a more elaborate ion trap mounting scheme was required.

The final design was dictated by the need to have complete, external adjustability of the ion trap in three dimensions with respect to the particle beam axis. A simple x-y-z translation stage to mount the ion trap was therefore designed and fabricated. The stage allows accurate positioning of the entrance hole in the trap to maximize the transport of the particle beam. The mounting flange that holds the stage was also modified to include three simple, O-ring sealed, rotary feedthroughs to provide the necessary adjustment controls. The final mounting system is shown in Figure 11b.

While the new mounting assembly was being fabricated, we attempted to align the final skimmer with the particle beam to complete the spatial distribution measurements. Although we had successfully used an acoustic alignment procedure with the first skimmer, it proved unsatisfactory for positioning of the second skimmer. Similarly, attempts to use a simple optical alignment method were also unsatisfactory. As an alternative we constructed a mechanical

alignment jig to provide the necessary positioning accuracy. Using this jig, we can reproducibly align the final skimmer to within 0.01 cm. With the second skimmer aligned, the final particle distribution measurements were completed before installing the ion trap assembly.

With alignment completed, final assembly of the pyrolysis-equipped ion trap on the translation stage could be completed, and the entire trap assembly has been mounted within the vacuum chamber. All the necessary electronics were interfaced with the ion trap and pyrolysis filament so that mass spectra of volatilized test particles could be measured.

### 3.2.5 Particle Beam Formation and Spatial Distribution

One important operational aspect of the sampler is the spatial distribution of particulates entering the ion trap. The size of the particulate "beam" will determine the size of the pyrolysis filament and hence the size of the hole that must be placed in the ion trap electrode. To determine this critical parameter, we designed an experiment to measure the spatial distribution using fluorescent latex particles. These particles have a uniform size and can easily be visualized by optical excitation. The sampler was interfaced to a vacuum pump to achieve the 50-Torr operating pressure, and the particle beam impinged on a glass slide coated with vacuum grease. After operation for a fixed length of time with a uniform particle loading (particles/$cm^3$ in the sampling chamber), the glass slide was removed and examined. A scanning densitometer was used to quantitate the spatial distribution. We also measured the particle flux from the generator (particles/$cm^3$) using 3.7-μm latex spheres. By combining this information with the carrier gas flow rate, we could estimate the length of time required to deposit a reasonable number of spheres on the target surface. We estimate that the amount deposited corresponds to much less than a monolayer so that the measured distribution will be due to the actual particle beam distribution and not to redistribution resulting from latex spheres impacting on other latex spheres. In other words, to a high probability, each latex sphere that hits the target surface will strike the vacuum grease coating and stick with unit probability.

A preliminary test was run using fluorescent latex spheres. After operation for several minutes (calculated to be sufficient time based on the known particle flux), there was no discernable accumulation of particles downstream of the sampling skimmers. By placing a collection screen near the vacuum pump outlet, we determined that essentially all the latex particles were being exhausted through the pump and not being sampled through the nozzle. Minor changes in the sampler design were then made to reduce this split ratio. In addition to measuring this distribution for a monodisperse sample, the experiment was repeated with a mixture of particle sizes to determine if there is a sampling bias as a function of size. The results of these experiments are discussed below, and they allowed completion of the pyrolysis filament design.

The basic concept of the experiment is to direct the particle beam at a target coated with an adhesive layer that would trap the particles for analysis. By using particles dyed with uv sensitive fluorescent colors, we can easily count the number of particles collected in a given exposure time. Our initial plans to use the standard vacuum-compatible grease (Apiezon) proved unworkable since the grease itself exhibited strong uv-induced fluorescence that masked the fluorescence from the latex spheres. Therefore, the first results were obtained by using a commercial adhesive-coated material ("Spots-o-Glue") designed for mounting SEM samples. The initial experiment with these mounts collected particles at the position of the first skimmer, 0.6 cm beyond the end of the particle delivery tube. After a 10-minute run, a 0.2-cm-diameter fluorescent spot was observed under uv excitation. Attempts to examine the particle distribution using both optical and electron microscopy proved unsuccessful because of the rough nature of the Spots-o-Glue surface.

Because of the problems associated with the use of the Spots-o-Glue, we investigated the use of other vacuum-compatible greases and found that ordinary silicon grease offered a suitable medium for collecting and viewing particles. After the first skimmer was installed and aligned, a silicon grease-coated slide was placed at the position of the second skimmer. Following a 28-

minute exposure to latex spheres, a weak 0.4-0.5-cm-diameter spot was observed. A second run produced a smaller spot (0.3-cm-diameter) as a result of reducing the nozzle-to-skimmer distance from 0.3 cm to 0.2 cm. Examination of the resulting particle distribution using an optical microscope equipped with uv excitation and fluorescence viewing filters showed a relatively uniform spread across the spot.

An example of the distribution observed through a blue filter is shown in Figure 12. The dark region in the lower left corner shows the sharply defined edge of the particle distribution. The full image also exhibited a smeared portion in the upper right corner that is not due to particles, but rather appears (under higher magnification) to be due to the spreading of the fluorescent dye into the silicon grease. It is likely that the particle beam retains some small amount of butanol, the solvent used to suspend the latex spheres for nebulization. Any excess solvent that is not removed in the expansion/desolvation region of the particle generator would reach the silicon grease surface and cause small amounts of the dye to run. We did observe that, when the nozzle was rotated, the smearing of the image also rotated, indicating that the source of the smearing is associated with the nozzle itself and not the skimmers or their alignment. Further investigation confirmed that the smearing is not due to any asymmetry in the particle beam, but rather to the method in which it is generated; hence it is not a problem that will be observed with an actual particle beam sampled from a stack.

Following the experiment described above using a monodisperse beam of latex particles, a second experiment was performed using mixtures of particles to investigate any bias in the sampling associated with particle size. By using particles dyed red (0.5 μm), green (1 μm), and blue (2.0 μm), we can easily distinguish their spatial distribution using the fluorescence microscope. The first tests using the mixed size beam were inconclusive because the ratio of 0.5:1:2.0 μm latex particles was not correct. An excess of red particles obscured the fluorescence, and some agglomeration was apparent, indicating that the overall concentration was too high.

A new mixture was prepared that corrected both these problems, and another set of experimental runs was completed. With the new mixture, runs were made at nozzle-skimmer distances of 0.1, 0.5, and 0.7 cm, each for 10- and 15-minute durations. A microscopic analysis of the resulting distributions showed that the 0.1- and 0.5-cm runs produce well focused spots, while the 0.7-cm run gave a diffuse spot. Also, the overall particle density appeared to be weaker than desirable for particle counting purposes. Because of these preliminary results, we repeated the measurements with a more concentrated mixture over a narrower nozzle-skimmer distance range of 0.2-0.5 cm.

Figure 13 shows the results of using a monodisperse beam of 0.482-μm blue particles to measure the spatial distribution of the particle beam. The photograph shows a well defined circular pattern with a diameter of approximately 0.08 cm. Figures 14 through 16 show the corresponding circular patterns measured using a 1:1:1 mixture of 2.00-μm (blue), 1.01-μm (green), and 0.508-μm (red) latex spheres. These three photographs were made from the same deposited spot, using three optical filters on the microscope.

The measured radial distribution of each size particle is plotted in Figure 17 for three separate runs. These data clearly show that the largest particles are more strongly focused near the center of the beam. While this is not surprising, we also observe that the total number of particles collected of each size is not the same. For example, the total number of the largest particles collected is approximately 150, while the corresponding total for the smallest particles is between 500 and 600. This disparity could reflect either a sampling bias or a bias in the particle beam generation. This uncertainty can be resolved by collecting particles at the exit of the particle beam generator nozzle. If that sample shows no bias, then the results in Figure 17 must have arisen from a bias in the sampling of the particles by the differentially pumped skimmer system.

Using an alignment jig previously developed, we successfully aligned the final particle beam-forming aperture with the other skimmers. We verified the alignment by collecting a particle sample on a coated foil positioned approximately 3.5 cm downstream from the final aperture.

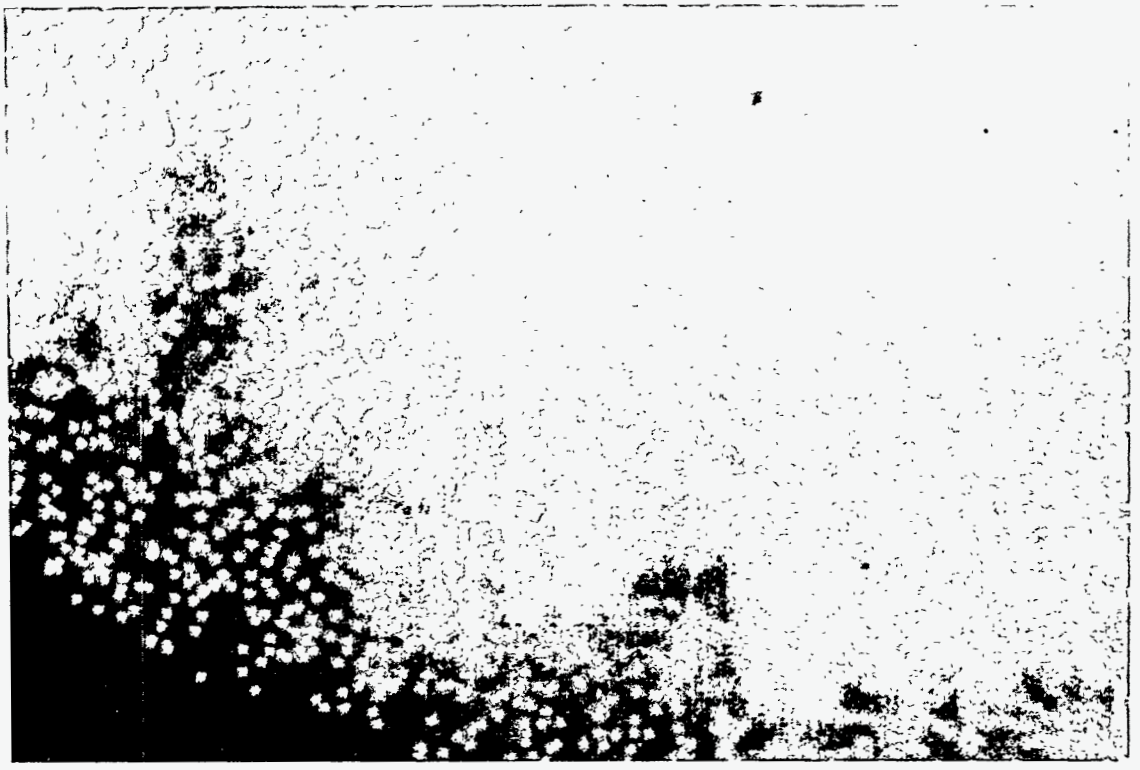

CP-4019-21

Figure 12. Optical microscope image of 2.7-μm-diameter fluorescent latex spheres observed under ultraviolet illumination.

The dark region in the lower left corner corresponds to the edge of the distribution.

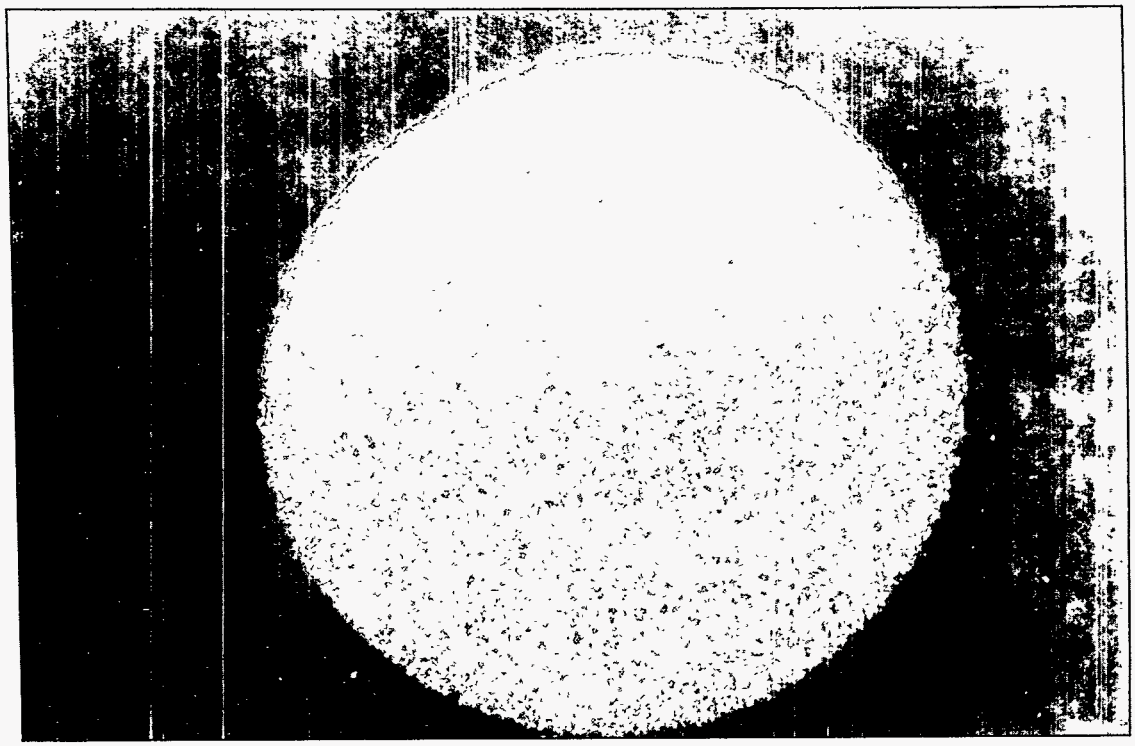

CP-4019-22

Figure 13. Photograph of 0.482-µm latex particles collected on a stainless steel foil coated with silicone grease.

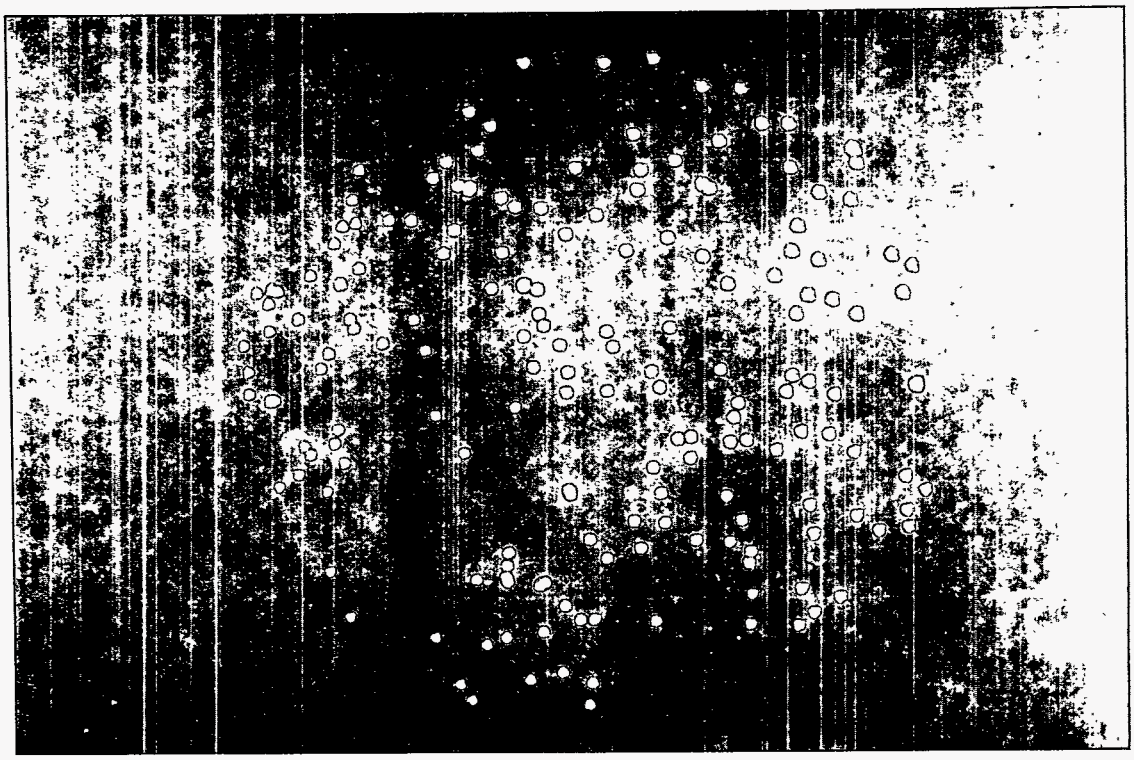

CP-4019-23

Figure 14. Photograph of 2.0-µm latex particles collected on a stainless steel foil coated with silicone grease.

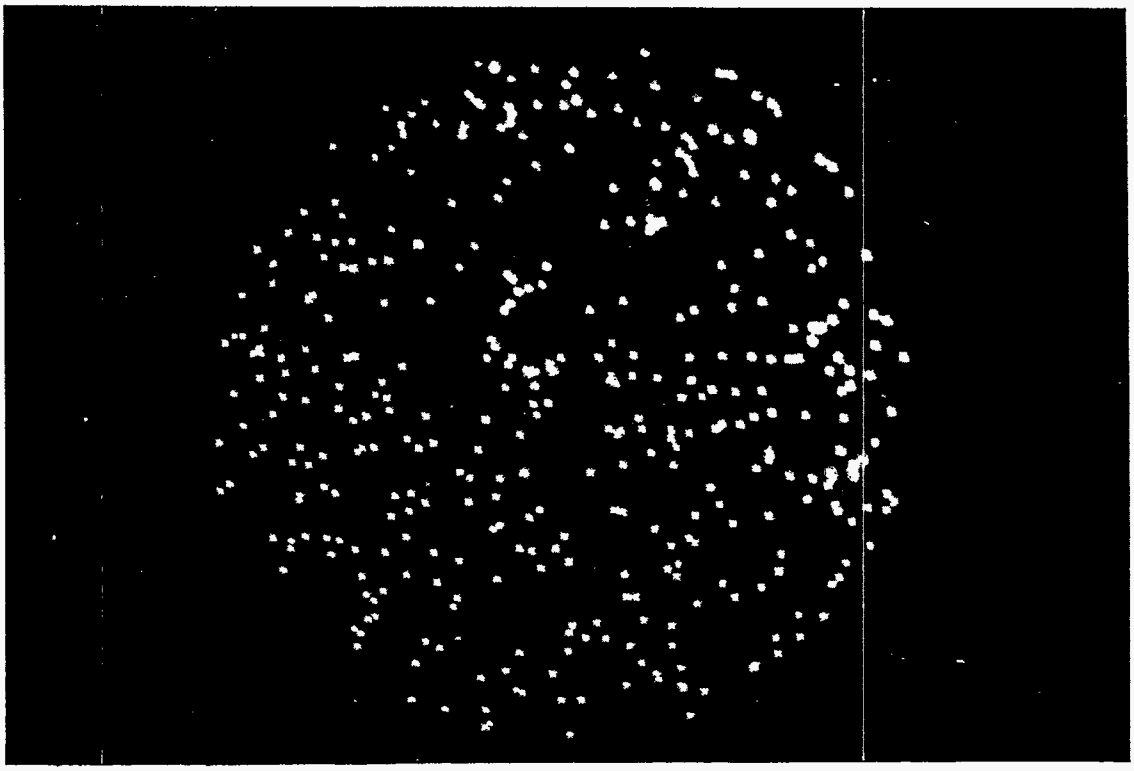

CP-4019-24

Figure 15. Photograph of 1.01-μm latex particles collected on a stainless steel foil coated with silicone grease.

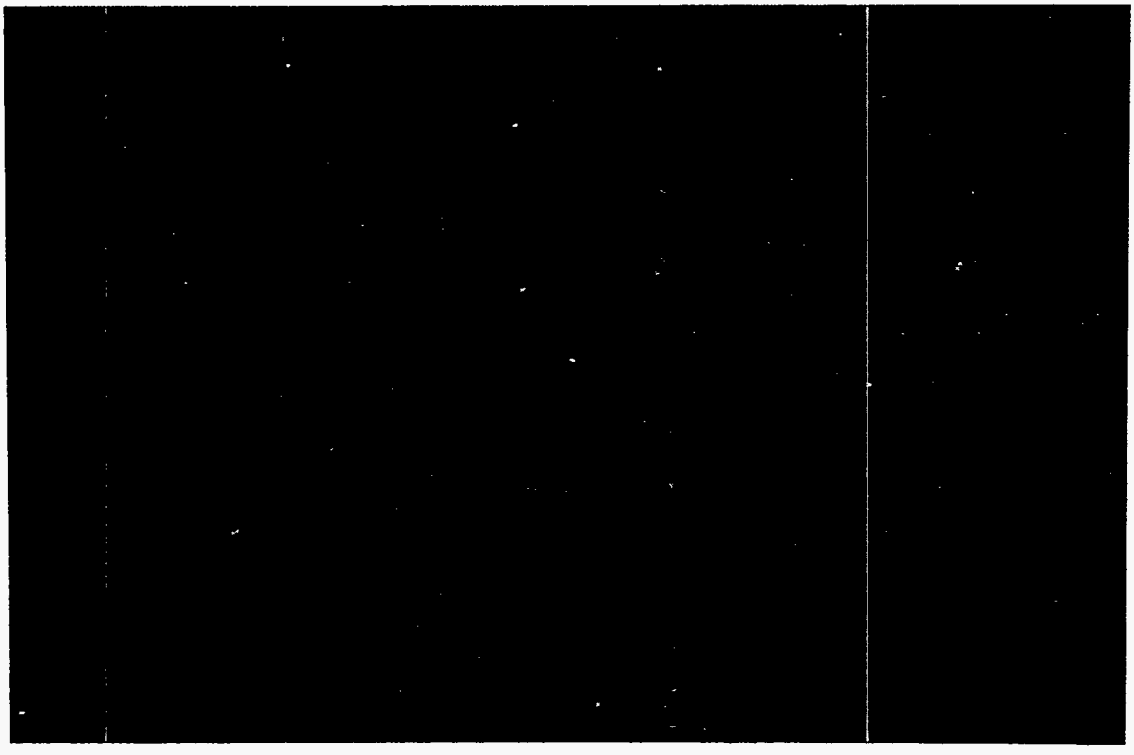

CP-4019-25

Figure 16. Photograph of 0.508-μm latex particles collected on a stainless steel foil coated with silicone grease.

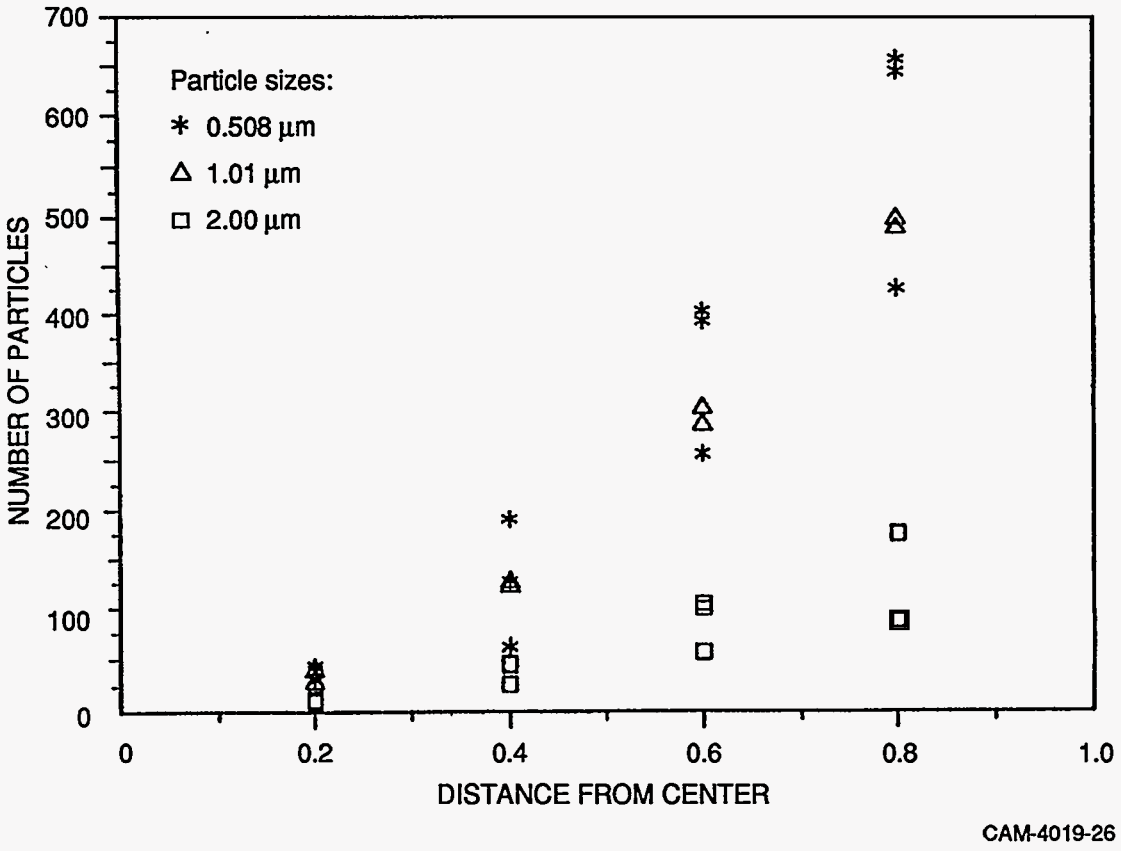


Figure 17. Measured radial distribution of latex spheres as a function of diameter.

The entire collection area has a diameter of 0.8 mm. Multiple runs are plotted for each size particles.

Using the same 1:1:1 mixture of 0.5-, 1.0,- and 2.0-μm diameter latex particles and the microscope equipped with uv-induced fluorescence detection, we measured the final beam size to be 0.078 cm. This beam size is smaller than the 0.2-cm-diameter entrance channel in the ion trap, indicating that we can increase the beam-defining aperture sizes to increase sensitivity as necessary.

The entire trap assembly was mounted within the vacuum chamber and aligned with the particle beam axis. The mounting process involved the complete assembly and testing of a positioning system that allows the trap to be aligned with the particle beam axis. This positioning and mounting system includes both the mechanical motion as well as the electrical connections between the vacuum flange and the ion trap itself. All the internal ion trap wiring was done using vacuum compatible materials

Once the ion trap electronics were installed, it was necessary to retune the rf to account for changes in the cable capacitance. After retuning, the ion trap operated normally, although the background mass spectrum showed significant outgassing by some of the polymer materials used to fabricate the ion trap positioning components. Several unsuccessful attempts were made to observe the mass spectrum of pyrolyzed latex particles introduced into the trap by the beam. Additional attempts to align the ion trap entrance channel with the particle beam in real time were also not successful. Because we had previously verified the alignment of the beam generation nozzle with both of the skimmers, it was clear that the ion trap was not aligned with the beam axis. To facilitate alignment of the beam axis with the ion trap, we then used an optical alignment procedure. The particle beam delivery system was temporarily removed and a small HeNe laser was used to define the beam line. The pyrolysis filament was removed from the trap to allow the light to pass completely through. We quickly discovered that the ion trap was rotated considerably from the correct straight line path. In other words, when the laser beam entered the ion trap channel, it did not exit through the pyrolysis filament opening. This misalignment would ensure that no particles would reach the filament.

After we discovered that the ion trap was rotated considerably from the correct straight line path, the trap was properly positioned. With the trap and particle beam aligned, we performed an experiment to detect the molecular beam formed by the expansion of the butanol/argon through the sampling nozzle. We expected that this molecular beam would provide a measurable mass spectrometric signal that was sharply peaked and spatially well-defined, corresponding to the optimum alignment of the ion trap entrance channel with the beam. Although we did note a slight increase in the signal that was attributable to the argon carrier gas, its magnitude was considerably smaller than expected, as was its broad spatial extent. Upon closer examination of the relative pressures in the first differential region and the ion trap region, it was apparent that conditions were not conducive to the formation of a true supersonic molecular beam. The primary difficulty appeared to be the excessive pressure (3-5 mTorr) in the region of the first sampling skimmer. Such a high pressure can easily lead to multiple gas collisions in the vicinity of the skimmer throat, with a significant loss of beam intensity through scattering.

To remedy this situation, we modified the apparatus so that the first differential pumping region could be maintained at a lower pressure. We placed the mechanical pumping system with a small diffusion pump (nominal pumping speed of 300 l/s). With the change in pumps for Region I, several of the vacuum design parameters required adjustments, as detailed below.

### 3.2.6 Vacuum System Pumping Calculations – Current Design

The following changes were made in the vacuum system component parameters:

1. 300 l/s diffusion pump replaces 5.6 l/s mechanical pump in Region II.
2. Orifice diameters:
   Nozzle ($A_{12}$) = 178 μm
   Skimmer ($A_{23}$) = 390 μm (commercially available skimmer)
   Skimmer ($A_{34}$) = 0.12 cm

For a nozzle diameter d = 178 μm and $T = T_0 \simeq 300$ K, the background pressure in Region II ($P_{II}$) is found to be

$$P_{II} = \frac{CP_0d^2}{S} \qquad \text{where} \quad P_0 = 50 \text{ Torr (assumed inlet pressure)}$$

$S \simeq 300$ l/s (diffusion pump speed)

$C = 21$ l/cm$^2$·s (constant for argon carrier gas)

$$P_{II} = \frac{(21 \text{ l/cm}^2\cdot\text{s})(50 \text{ Torr})}{300 \text{ l/s}} d^2$$

$$= 3.5\, d^2 = \boxed{1.1 \times 10^{-3} \text{ Torr}}$$

$$\text{Mach disk location} = X_M = (0.67)\left(\frac{P_0}{P_b}\right)^{\frac{1}{2}} (d)$$

$$= (0.67)\left(\frac{50}{1.1 \times 10^{-3}}\right)^{\frac{1}{2}} (1.78 \times 10^{-2} \text{ cm})$$

$$X_M = 2.52 \text{ cm}$$

In Region III, the revised parameters are $P_0$ (Region I) = 50 Torr

$P_{II} = 1.1 \times 10^{-3}$ Torr

Nozzle $A_{12}$ to skimmer $A_{23}$ distance = 0.3 cm

$$\text{Number density at skimmer } A_{23} = n = (0.161)\,(3.24 \times 10^{16} \frac{\text{atoms}}{\text{cm}^3/\text{Torr}})\,(50 \text{ Torr})\left(\frac{0.0178 \text{ cm}}{0.3 \text{ cm}}\right)^2$$

$$= 9.2 \times 10^{14} \text{ atoms/cm}^3$$

For a velocity of $v \simeq 4 \times 10^4$ cm/s, the flux at skimmer $A_{23} = nv$

$$\simeq 3.7 \times 10^{19} \text{ atoms/cm}^2\cdot\text{s}$$

The numbers of atoms passing through $A_{23}$ into Region III is then

$$(3.7 \times 10^{19} \text{ atoms/cm}^2\text{·s}) \left(\frac{\pi}{4}\right) (0.0390)^2$$

$$\simeq 4.4 \times 10^{16} \text{ atoms/s}$$

The throughput contribution from the molecular beam ($Q_{III,MB}$) is thus

$$Q_{III,MB} = \frac{4.4 \times 10^{16} \text{ atoms/s}}{3.24 \times 10^{19} \text{ atoms/l·Torr}} \simeq 1.4 \times 10^{-3} \text{ Torr·l/s}$$

while the throughput associated with diffusion across $A_{23}$ ($Q_{III,D}$) is

$$Q_{III,D} = (1.1 \times 10^{-3} \text{ Torr}) (9.15) (0.0390 \text{ cm})^2 \simeq 1.5 \times 10^{-5} \text{ Torr·l/s}$$

The combined throughput in region III ($Q_{III} = Q_{III,MB} + Q_{III,D}$) $\simeq 1.42 \times 10^{-3}$ Torr l/s. Therefore, the estimated pressure in Region III is

$$P_{III} \simeq \frac{1.42 \times 10^{-3} \text{ Torr l/s}}{135 \text{ l/s}} \simeq \boxed{1.0 \times 10^{-5} \text{ Torr}}$$

In Region IV, the revised parameters are Orifice diameter ($A_{34}$) = 0.12 cm
$A_{23}$ to $A_{34}$ distance = 6.41 cm

Solid angle of skimmer $A_{23}$ (viewed from nozzle) $= \frac{\pi/4 \ (0.039 \text{ cm})^2}{(0.3 \text{ cm})^2} = 1.33 \times 10^{-2}$ steradians

The beam flux exiting skimmer $A_{23} = \frac{4.4 \times 10^{16} \text{ atoms/s}}{1.33 \times 10^{-2} \text{ steradians}} = 3.3 \times 10^{18}$ atoms/steradian·s

Solid angle of skimmer $A_{34}$ (viewed from nozzle) $= \frac{\pi/4 \ (0.12 \text{ cm})^2}{(6.41 \text{ cm} + 0.3 \text{ cm})^2} \simeq 2.5 \times 10^{-4}$ steradians

The flux through skimmer $A_{34} = (3.3 \times 10^{18} \text{ atoms/s steradian}) (2.5 \times 10^{-4} \text{ steradians})$
$= 8.25 \times 10^{14}$ atoms/s

The throughput contribution due to the molecular beam is

$$Q_{IV,MB} = \frac{8.25 \times 10^{14} \text{ atoms}}{3.24 \times 10^{19} \text{ atoms/l Torr}} \simeq 2.5 \times 10^{-5} \text{ Torr l/s}$$

while the corresponding throughput associated with the diffusion across $A_{34}$ is

$$Q_{IV,D} = (1.0 \times 10^{-5} \text{ Torr}) (9.15) (0.12 \text{ cm})^2$$
$$\simeq 1.3 \times 10^{-6} \text{ Torr l/s}$$

Combining throughputs $Q_{IV,MB}$ and $Q_{IV,D}$ gives

$$Q_{IV} \simeq 2.63 \times 10^{-5} \text{ Torr l/s}$$

Therefore, the estimated pressure in Region IV is

$$P_{IV} \simeq \frac{2.63 \times 10^{-5} \text{ Torr l/s}}{220 \text{ l/s}} \simeq \boxed{1.7 \times 10^{-7} \text{ Torr}}$$

The change in pumping required some minor modifications to the vacuum housing, including the addition of an ionization gauge that will allow a better measure of the pressure in this region. Preliminary tests of the system following these changes indicated that the molecular beam formation process was considerably enhanced. Under the new conditions, we are able to mechanically scan the position of the ion trap with respect to the anticipated beam axis and observe a distinct and sharp maximum in the argon signal measured by the mass spectrometer. We also know that the pressure in the first differential pumping region is low ($\lesssim 1 \times 10^{-3}$ Torr with the beam running) to avoid the scattering losses previously encountered.

We began testing the modified system with the latex particle beam. Initially, we operated the beam for a short period of time with the pyrolysis filament off to accumulate particles on its surface. The filament was then flash heated while observing the ion trap signal. The reason for using this mode of operation rather than looking for single particle events is our lack of ability to externally trigger the ion trap scan. After collecting latex particles for a minute, we could readily observe their characteristic mass spectrum once the pyrolysis filament was heated above their volatilization temperature.

Next, we operated the system in real-time; that is, we observed the mass spectra continuously while allowing latex particles to impact upon a heated pyrolysis filament. Although we were not triggering the mass scans in synchrony with the particle arrival, we anticipated that enough accidental coincidences would occur to allow us to directly observe particles. In fact, there were occasional mass scans with clear evidence of volatilized latex particles. The frequency of these observed mass scans was relatively low due to the apparently poor efficiency with which we are transporting the particles through the sampling system and into the ion trap. Nonetheless, this is clear proof that the basic concept of *in-situ* pyrolysis and mass spectrometric analysis of externally sampled particles is a viable means of providing a real time stack monitor.

### 3.2.7 Particle Sampling Efficiency and Sampling Bias

A continuing difficulty with the present system is the poor particle sampling/transmission efficiency through the various stages of the instrument. Since an efficient and unbiased sampling system is essential to the ultimate success of this approach, we began a systematic check of each stage of our sampling system. These tests include the collection of particles at different locations throughout the system and a comparison of the absolute number of particles, their spatial distribution as a function of size (using a mixture of 0.5-, 1.0-, and 2.0-μm particles), and the uniformity of those distributions.

The first test involved collecting particles using an in-line filter just before the nozzle that generates the "beam." Particles were collected for a fixed period of time, then analyzed using an optical microscope equipped with uv illumination. The particles are color coded by using uv absorbing dyes to allow each size particle to be individually counted. Particles were counted in quadrants to provide some measure of spatial uniformity. The results of that experiment are given in Table 6.

**Table 6. Spatial Distribution of Latex Particles Collected before Beam Formation**

| Quadrant | 2.0 μm (blue) | 1.0 μm (green) | 0.508 μm (red) | 2 μm/1 μm |
|---|---|---|---|---|
| I | 9 | 24 | > 40 | 1 : 2.7 |
| II | 13 | 40 | – | 1 : 3.1 |
| III | 15 | 44 | – | 1 : 2.9 |
| IV | 18 | 53 | > 80 | 1 : 2.9 |

Note that the density of 0.5-μm (red) particles was so high that it was not possible to accurately determine their number. This result does show, however, that starting with a 1:1:1 mixture of particle sizes introduces a significant degree of bias in the nebulization process used to introduce the particles into the sampled gas stream. This bias is not particularly important, since it is an artifact of the particle introduction method and not of the particle sampling method. In a real world situation, the particle generation method is fixed by the process being monitored. Nonetheless, these results show several key features: (1) the spatial distribution is reasonably uniform (at least with respect to the two larger sized particles), and (2) the ratio of 2-μm to 1-μm particles is constant across the particle stream.

The next experiment involved collecting particles 0.06-cm downstream of the orifice plate (0.025-cm-diameter orifice). The result of that experiment is shown in Table 7.

**Table 7. Spatial Distribution of Latex Particles Collected after 0.025-cm Orifice**

| Run | 2.0 μm (blue) | 1.0 μm (green) | 0.508 μm (red) | 2μm/1μm/.5μm |
|---|---|---|---|---|
| I | 175 | 487 | 642 | 1 : 2.8 : 3.7 |
| II | 174 | 496 | 655 | 1 : 2.8 : 3.8 |

Interestingly, the ratio of 2-μm to 1-μm particles remains approximately the same, showing no sampling bias. However, since the number of 0.5-μm particles is clearly much smaller than that collected before the orifice plate, there appears to be a significant sampling bias against the smallest diameter particles. Despite this bias, the absolute numbers of smaller particles is large owing to their dominance in the original sample stream.

As a result of the changes in the pumping system described previously, we changed the orifice plate from the original 0.025-cm diameter to 0.0125-cm diameter to reduce the gas loading on the intermediate pumping region. The smaller orifice plate was used during the real time measurements described at the beginning of this report. Hence, we repeated the particle collection experiment with the smaller orifice in place. Those results are given in Table 8 and should be compared with the corresponding results in Table 7.

It is apparent that both the number of particles traversing the smaller orifice is considerably less that can be accounted for by geometry, and a very significant sampling bias has been introduced, allowing far fewer of the larger particles to pass into the next vacuum region. A possible cause is discussed below. A final experiment was performed in which particles were collected after the final skimmer. The result of that experiment is presented in Table 9.

**Table 8. Spatial Distribution of Latex Particles Collected After 0.0125 cm Orifice**

| Run | 2.0 μm (blue) | 1.0 μm (green) | 0.508 μm (red) | 2μm/1μm |
|---|---|---|---|---|
| I | 7 | 112 | >> 1 μm | 1 : 16 |
| II | 3 | 68 | >> 1 μm | 1 : 23 |

**Table 9. Spatial Distribution of Latex Particles Collected After Final Skimmer**

| Run | 2.0 μm (blue) | 1.0 μm (green) | 0.508 μm (red) | 2μm/1μm |
|---|---|---|---|---|
| I | 26 | ~300 | > 1 μm | 1 : 12 |

It appears that little additional sampling bias is introduced by the skimmer; thus, we would conclude from these experiments that the main difficulty lies in the beam formation dynamics associated with the first orifice plate. Following these measurements and the real-time experiments described above, we removed the 0.0125-cm orifice and examined it for particle buildup. This examination showed that a significant deposit of particles had formed on the inside of the orifice channel itself. The orifice plates have a thickness of approximately 0.025 cm, so that the 0.0125-cm-diameter orifice actually is a tube with an aspect ratio (length to diameter) of 2:1. Although nozzles with this aspect ratio are routinely used to generate gaseous molecular beams efficiently, this large aspect ratio appears to result in an early expansion *within* the channel, leading to the observed deposit. On the other hand, since the 0.02- cm-diameter orifice plate has an aspect ratio of ~1:1, it does not appear to suffer from the same difficulty. The major drawback to using the larger orifice is the increased gas load experienced by the intermediate vacuum region. Rather than use the larger orifice, it may prove useful to reduce the thickness of the 0.0125-cm orifice until it also has a 1:1 aspect ratio.

Our next experiments were designed to elucidate which of the various stages of the instrument causes the greatest losses. These tests involved the collection of particles at different locations throughout the system and a comparison of the absolute number of particles, their spatial distribution as a function of size, and the uniformity of those distributions. Particles were collected for a fixed period of time, then analyzed using an optical microscope equipped with uv illumination. The particles are color coded using uv absorbing dyes to allow each size particle to be individually counted (1.01-μm green, 2.0-μm blue, and 2.87-μm red particles were used). The results of these experiments are described in Table 10.

The primary test mixture was made by first placing equal weights of each size particle in separate containers with 100 mL of butanol in each. The particle weight was 1% of the total in each sample. Since the density of each latex particle is the same (0.9 g/cm$^3$), the actual mass of each particle size is given by their volume times their density, as shown below.

**Table 10. Primary Test Mixture Composition**

| Particle Size (μm) | Volume ( $cm^3$) | Mass (g) |
|---|---|---|
| 1.01 μm - green | $4.05 \times 10^{-13}$ | $3.64 \times 10^{-13}$ |
| 2.0 μm - blue | $3.14 \times 10^{-12}$ | $2.83 \times 10^{-12}$ |
| 2.87 μm - red | $9.28 \times 10^{-12}$ | $8.35 \times 10^{-12}$ |

The 1:8:23 ratio of these mass values provides the necessary proportions of each size particle to produce a 1:1:1 mixture. The actual mixture is made by combining 2, 16, and 46 drops of each solution in 100 mL of butanol. The absolute number of green particles, for example, is thus given by

$$2 \text{ drops} \times \frac{1 \text{ mL}}{20 \text{ drops}} \times \frac{1 \text{ cm}^3}{\text{mL}} \times \frac{0.01 \text{ g}}{\text{particle}} \times \frac{1 \text{ particle}}{3.64 \times 10^{-13} \text{ g}} = 2.8 \times 10^9 \text{ particles}$$

The corresponding particle delivery rate is found from this value and the flow rate

$$\frac{2.8 \times 10^9 \text{ particles}}{100 \text{ mL butanol}} \times \frac{0.7 \text{ mL}}{\text{min}} = 2.0 \times 10^7 \text{ particles/min}$$

Our first experiments investigated the relationship between the nozzle diameter and the particle generation bias. The original system design used a 0.0125-cm diameter orifice and produced a sample generation bias of 10-20 between the 1- and 2-μm particles. Switching to a 0.0178-cm-diameter orifice reduced this bias to 1.5, as summarized in Table 11.

**Table 11. Sampling Bias with Particle Size**

| Orifice Size (cm) | 1.0 μm (green)/2.0 μm (blue) | 1.0 μm (green)/2.87 μm (red) |
|---|---|---|
| 0.0125 | 10-20:1 | – |
| 0.0178 | 1.5:1 | 3:1 |

The use of a larger orifice has a significant effect on the particle generation bias, however, at the cost of increased gas loading on the sample introduction portion of the instrument. While the bias for the 2.87-μm particles is higher than for the 2.0-μm particles, it is unknown if the use of a larger orifice had a measurable effect.

Measurements were next made after the skimmer and after the final orifice plate just before entering the ion trap mass spectrometer. Those results are given in Table 12.The corresponding efficiency values are listed in Table 13.

These results show that, although the particle generation process results in only a modest size bias of 3:1.5:1 for 2.87-, 2.0-, and 1.0-μm-diameter particles, a significant bias (31:10:1) is apparent after the final orifice plate. The reasons for this size bias are unknown at present. The beam diameter is estimated to be 0.4 cm at the point where the particle beam reaches the final 0.15 cm diameter orifice. Thus, approximately 37% of the beam should be transmitted into the final vacuum region based solely on geometric considerations assuming perfect alignment. The possibility of some misalignment is being investigated.

**Table 12. Particle Collection at the Ion Trap Entrance**

| Particle Size (∝μ) | Average Number Entering nozzle/min | Average Number Collected after Skimmer | Average Number Collected after Final Orifice Plate |
|---|---|---|---|
| 1.01 μm - green | $2.23 \times 10^3$ | 43 | 31 |
| 2.0 μm - blue | 1066 | 25 | 10 |
| 2.87 μm - red | 914 | 13 | 1 |

**Table 13. Particle Collection Efficiency**

| Particle Size (μm) | Efficiency after Skimmer (%) | Efficiency after Final Orifice Plate (%) |
|---|---|---|
| 1.01 μm - green | 1.9 | 1.4 |
| 2.0 μm - blue | 2.3 | 0.9 |
| 2.87 μm - red | 1.4 | 0.1 |

It is interesting that, with the present configuration, $>10^4$ particles of each size are lost in the generation process; the majority are presumably pumped away. Moreover, given the present configuration, the particle arrival rate at the ion trap mass spectrometer is somewhat less than 1 particle/s (42 particles/min on average).

### 3.2.8 Organic Vapor Detection

A semipermeable membrane interface is used to separate the vapor and particulate streams for independent analysis by the two ion trap mass spectrometers. This membrane interface utilized a separate ion trap mass spectrometer. This instrument was an unmodified Finnigan model ITD800. Since it was unmodified, it lacked the axial modulation capability of the instrument used for the particulate testing. Without axial modulation, the overall instrumental sensitivity was less than that of a newer, modified device. The membrane inlet consisted of a small disk (0.8 cm diameter) of dimethylsilicon supported by a high transmission screen.

As diagrammed in Figure 18, vapors at atmospheric pressure were drawn across the surface of the membrane by a small diaphragm pump. Organic vapors preferentially permeate through the membrane, thus giving rise to an enhanced concentration on the back (low pressure) side. These vapors are then directly introduced into the ion trap volume through the GC inlet port drilled through the ring electrode. Normal 70-eV electron impact mass scans were performed. The sample vapors are generated using a 1-liter exponential dilution flask .

A known volume of organic solvent headspace vapor is injected into the heated flask where it mixes with a preheated nitrogen or argon carrier gas stream. The resulting homogeneous vapor mixture is drawn across the heated membrane inlet. The membrane temperature is maintained at an elevated level to prevent condensation of vapors and to enhance and adjust the permeation rate. For a given constant carrier gas flow rate, the concentration in the input stream at any time is given by the simple exponential decay function,

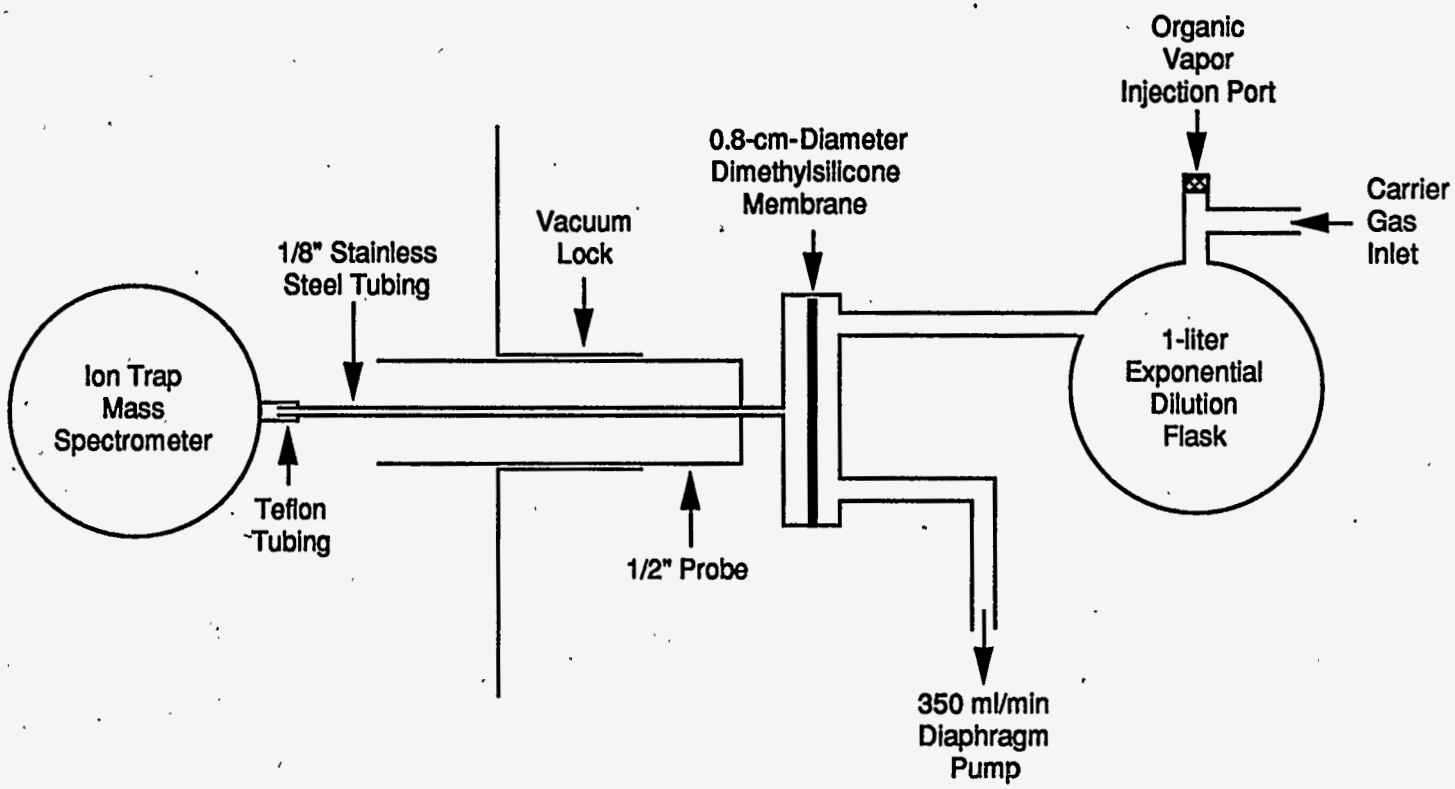


Figure 18. Membrane vapor inlet and exponential dilution flask interfaced with an ion trap detector. This configuration was used to determine the limits of detection for various organic vapors.

$$C = C_0 e^{-(t/t_0)} \quad (1)$$

where $C_0$ is the initial concentration of the organic vapor and $t_0$ is the measured time constant of the flask (volume/flow rate).

By measuring the ion signal for the vapor of interest as a function of time, we can obtain an absolute sensitivity value for the combined membrane inlet/ion trap system. Figure 19 shows typical ion trap data for toluene recorded using this approach. In the upper curve, the toluene signal is plotted as a function of time, with the injection point ($t_0$) clearly evident as the abrupt rise from the baseline. The signal level actually represents the sum of ion intensities between 90 amu and 93 amu. The lower figure shows a typical full mass scan for toluene. Using the known vapor pressure of toluene and the injected volume (100 µl), we calculate the absolute concentration of toluene in the vapor stream passing over the membrane to be 3.7 ppm. Thus, the maximum observed ion intensity corresponds to this toluene concentration. The concentration at any later time can be readily determined using equation (1). Representative values are shown in the upper curve of Figure 19.

Figures 20 through 22 show the measured data for carbon tetrachloride, trichloroethylene, and naphthalene. Note that the naphthalene signal is considerably weaker than the others since naphthalene is a solid at room temperature and hence has a much lower headspace vapor. To partially compensate, the injection volume was increased to 500 µl. Table 14 lists the estimated limits of detection (LOD) for these four compounds as well as the measured signal-to-noise ratios (S/N) at three different membrane temperatures.

**Table 14. S/N Ratios and Limits of Detection Using the Membrane Inlet**

| Compound | LOD (ppb) | Membrane Temperature (°C) | | | Ions Monitored |
|---|---|---|---|---|---|
| | | 22-25 | 41-50 | 95-115 | |
| Toluene | 25 | 4.3 | 4.1 | 1.7 | 90–93 |
| Carbon tetrachloride | 78 | 5.6 | 3.2 | 2.5 | 117–119 |
| Trichloroethylene | 97 | 5.5 | 2.6 | 1.4 | 95–97 |
| Naphthalene | 3 | 5.8 | 6.4 | 4.5 | 127,128 |

The LODs calculated from the ion trap/membrane data correspond to the concentration at which the S/N ratio falls below 3. Although the results in Table 14 indicate that this configuration provides very high sensitivity for typical organic vapors, the LODs could be improved by (1) using an ion trap with axial modulation, (2) increasing the size of the membrane, (3) optimizing the membrane inlet design, and (4) adjusting the sample flow rate.

### 3.2.9 Organic Analysis Using Field Ionization

Although the ion trap mass spectrometer normally uses electron impact (EI) ionization, it is not necessarily the optimum technique for the analyzing complex organic mixtures such as might be encountered in an incinerator stack. While several other ionization methods are potentially applicable to organic vapor detection, we selected field ionization (FI). Like chemical ionization (CI), FI is characterized as a "soft" ionization technique. Typical FI spectra are dominated by the parent ion and thus give valuable molecular weight information.

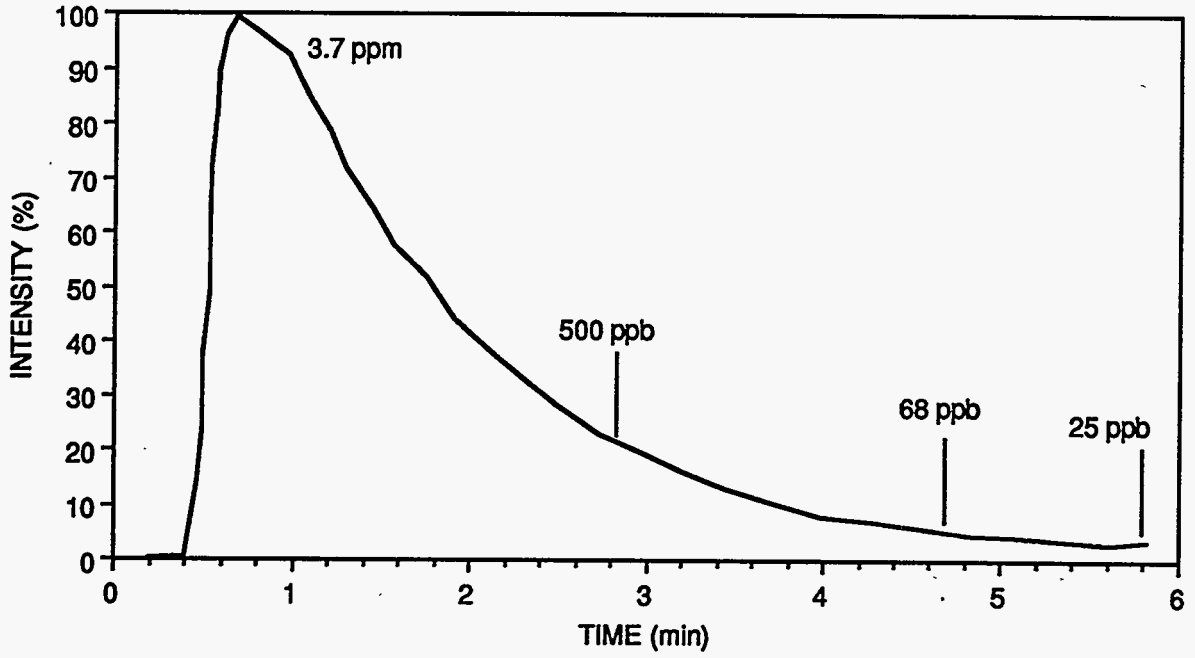


(a) Exponential dilution signal.

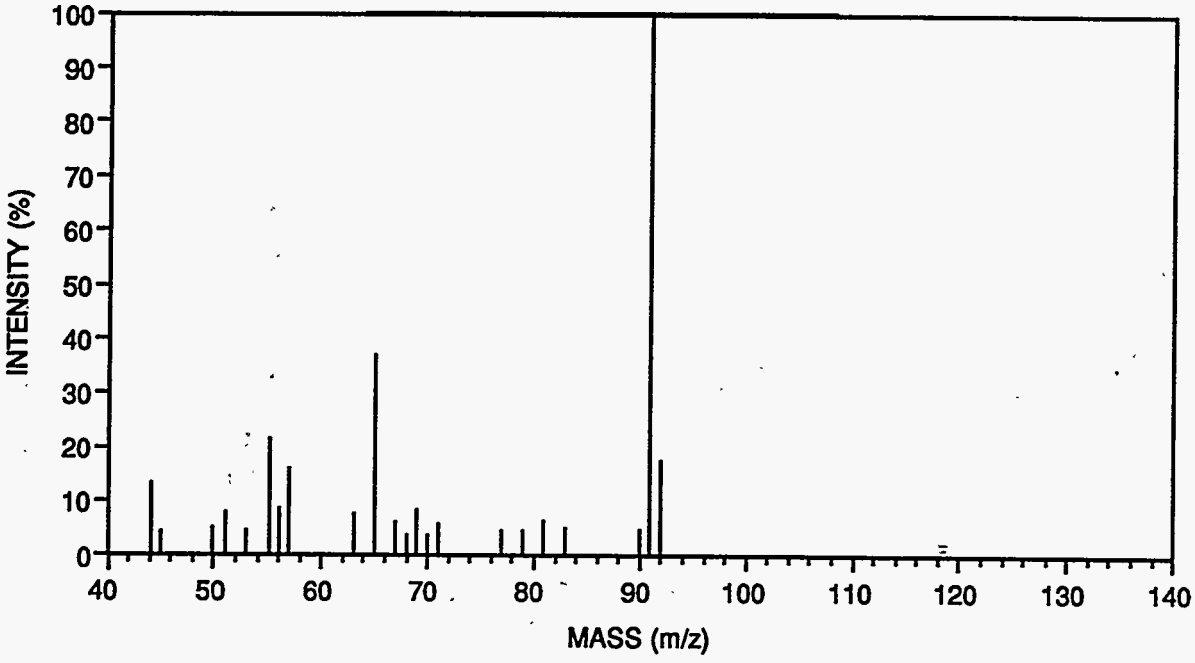


(b) Full scan mass spectrum.

CAM-4019-28

Figure 19. Limit of detection data for toluene.
Total flow over the membrane was 1 liter/minute using nitrogen carrier gas.

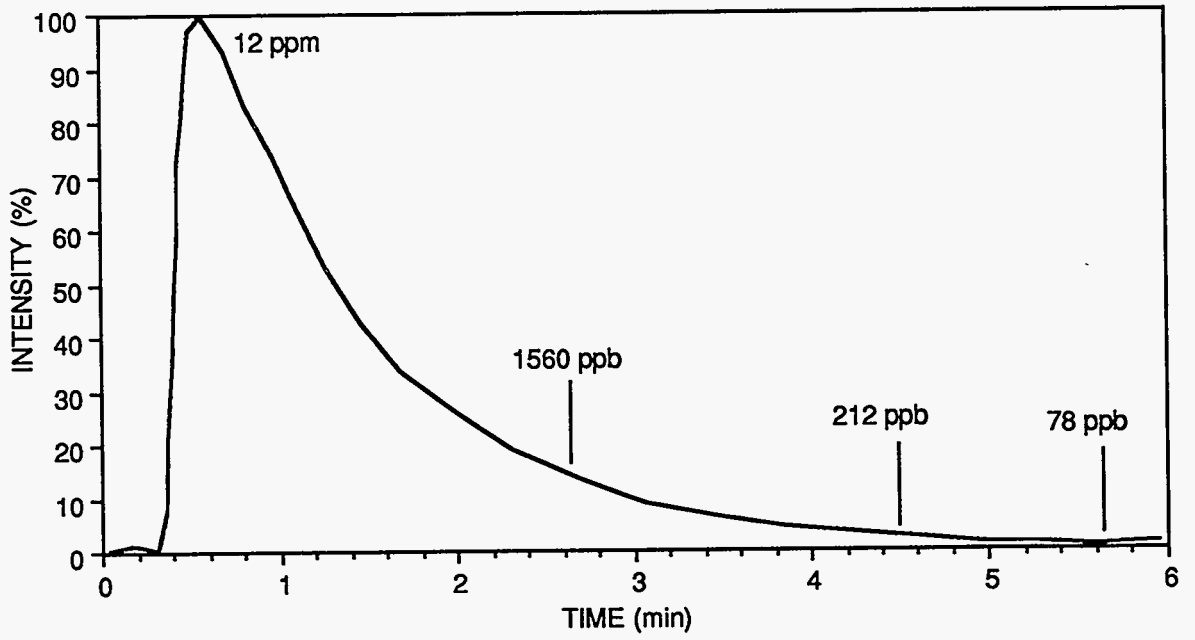


(a) Exponential dilution signal.

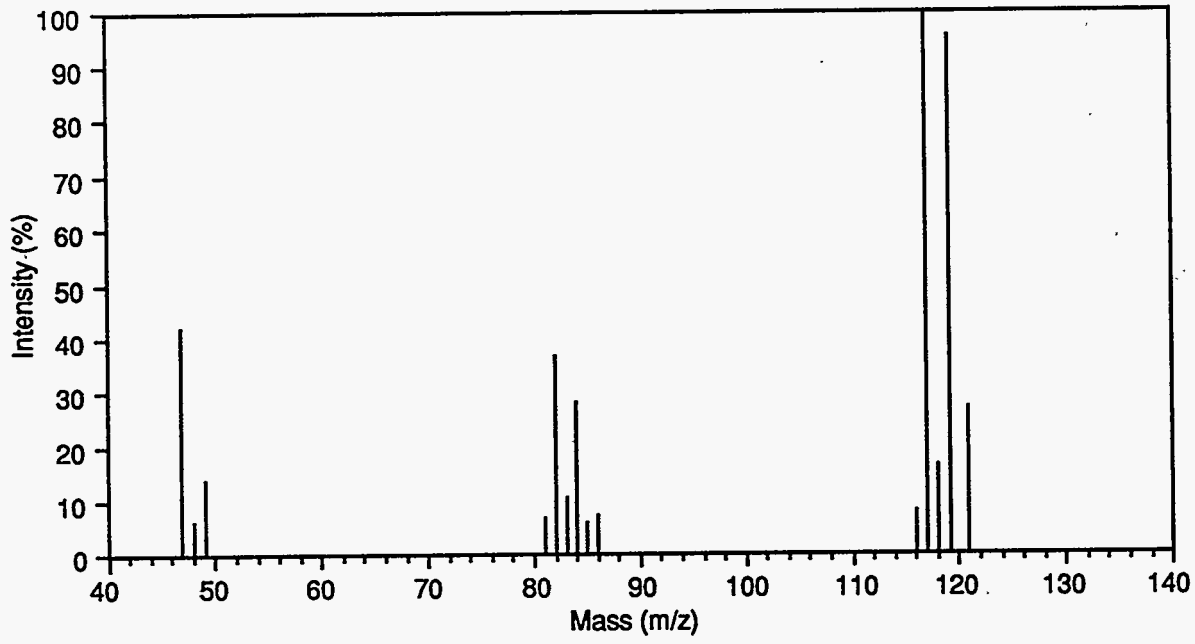


(b) Full scan mass spectrum.

CAM-4018-29

Figure 20. Limit of detection data for carbon tetrachloride.

Total flow over the membrane was 1 liter/minute using nitrogen carrier gas.

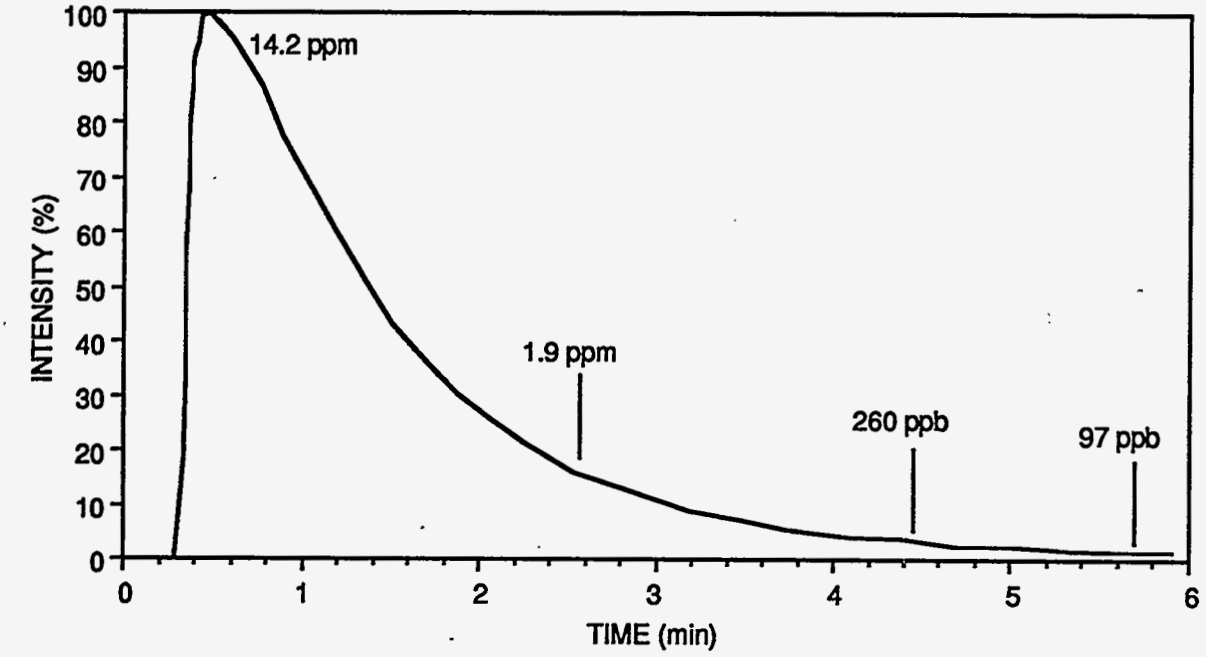


(a) Exponential dilution signal.

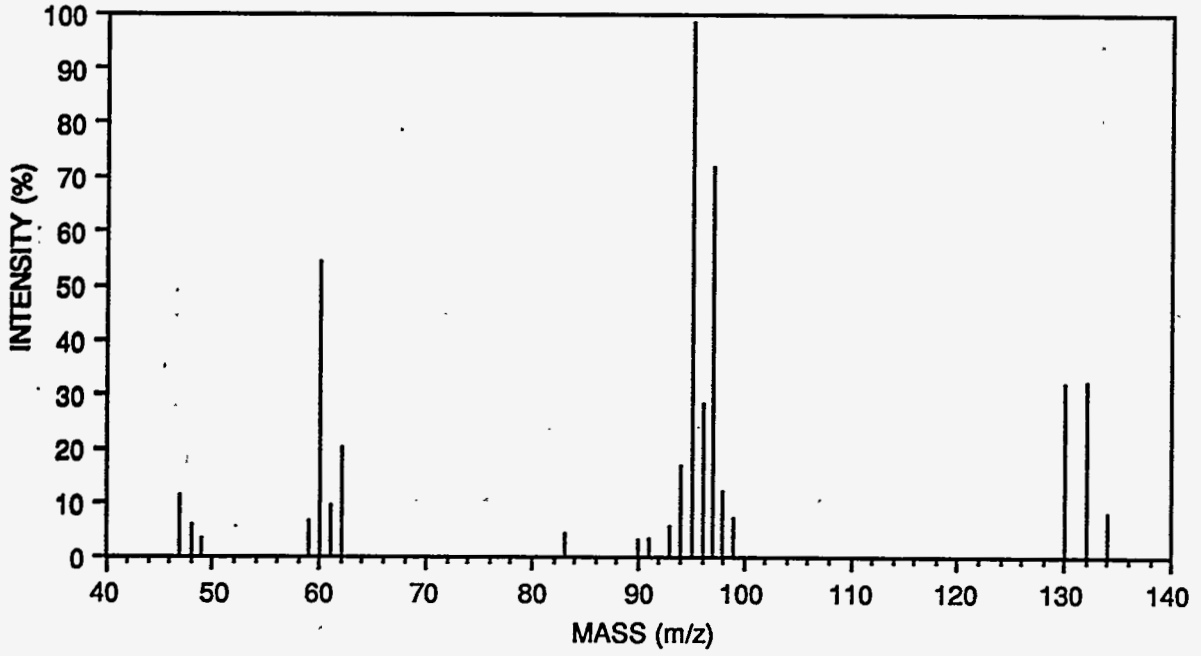


(b). Full scan mass spectrum.

CAM-4019-30

Figure 21. Limit of detection data for trichloroethylene.

Total flow over the membrane was 1 liter/minute using nitrogen carrier gas .

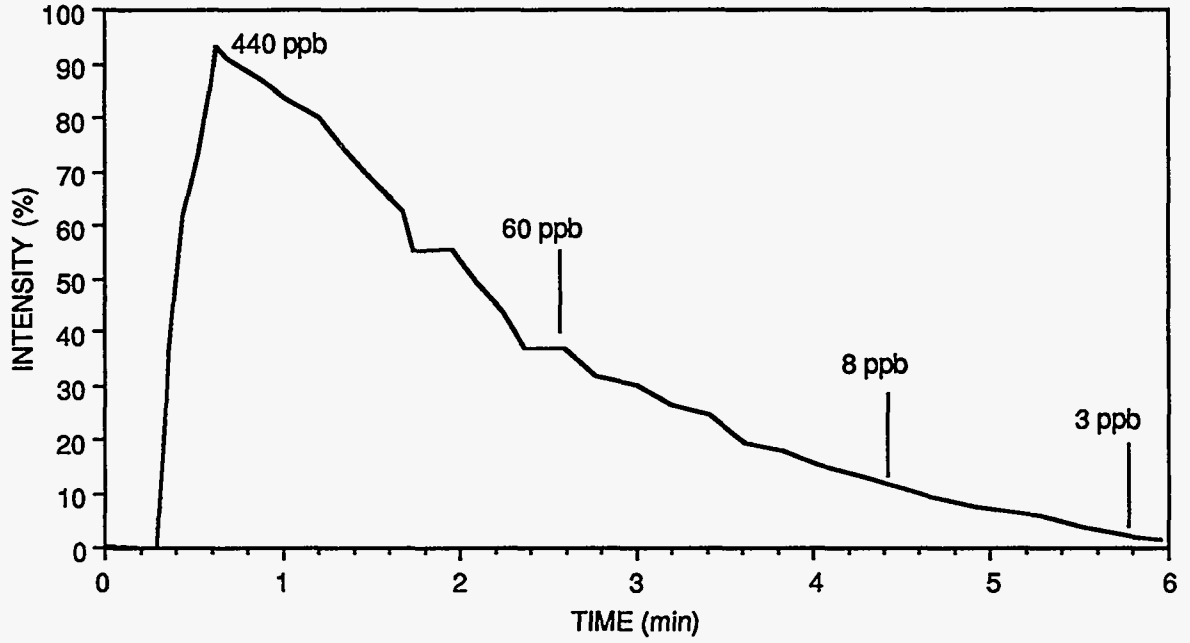


**(a)** Exponential dilution signal.

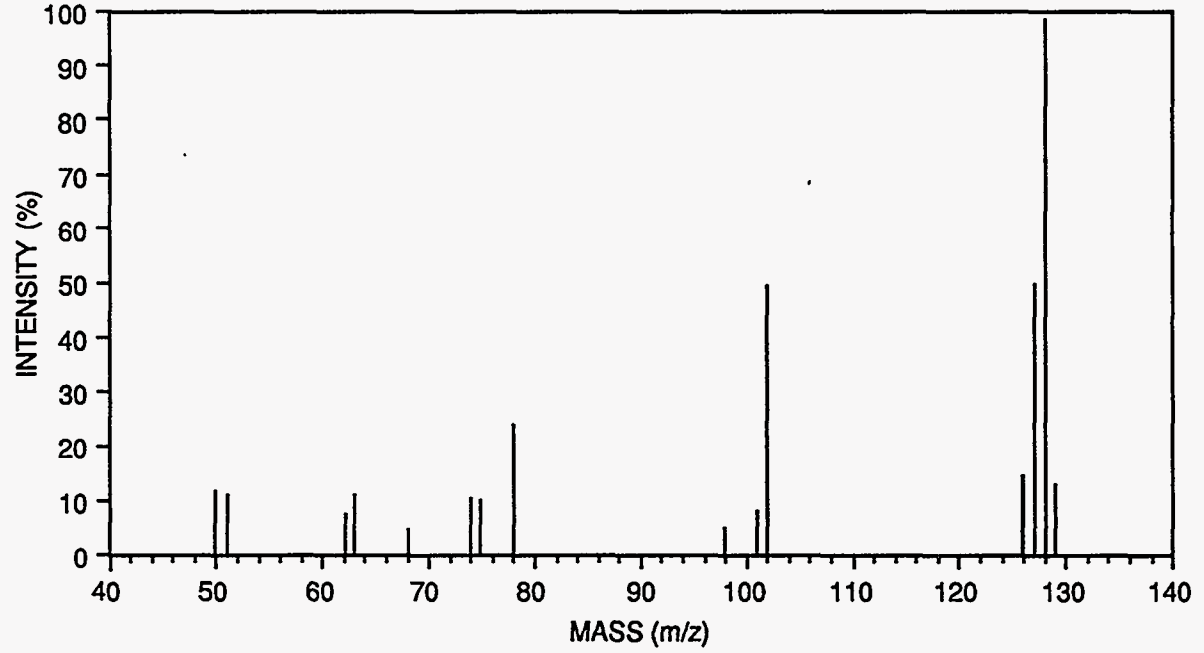


**(b)** Full scan mass spectrum.

CAM-4019-31

Figure 22. Limit of detection data for naphthalene.

Total flow over the membrane was 1 liter/minute using nitrogen carrier gas .

The operation of an FI source is fundamentally different from that of EI, CI, or atmospheric pressure ionization sources. To produce field ionization, the analyte molecules must be subjected to an electric field with a strength of $10^7$ to $10^8$ V/cm. Under these conditions, a valence electron tunnels from the molecule into the conduction band of the field ionizer to produce the $M^+$ ion. The nascent ion acquires only minimal internal excitation during this process, thereby avoiding fragmentation via unimolecular decomposition. Field ionization has found widespread use in the analysis of complex mixtures of hydrocarbon materials because it produces readily interpreted spectra.

One of the principal limitations of FI has been the reproducible generation of FI sources. A number of techniques have been investigated over the years, including the so-called volcano-style source developed by Mr. C. A. Spindt of SRI. A scanning electron micrograph of this microfabricated source is shown in Figure 23. The molecules of interest are constrained by the source geometry to pass through the 20-μm-diameter throat of the volcano and into the region of high field strength. The requisite electric field strengths are produced by submicroscopic carbon dendrites along the rim of the volcano, clearly visible in the lower portion of Figure 23. When a modest potential of 1.5 to 2.5 kV is applied between these structures and a closely spaced counter electrode, abundant field ionization is observed.

Despite its small physical dimensions, the volcano-style field ionization source is very rugged and reliable. When mounted in a suitable support structure, the device has the mechanical strength of any normal silicon microfabricated component (such as integrated circuits). Furthermore, the carbon dendrites that form along the rim of the volcano are actually pyrolytic graphite structures that are extremely robust and can withstand repeated exposures to air, mechanical vibration, thermal cycling, and so forth. When used for organic vapor analyses following a membrane inlet such as proposed here, these sources exhibit operational lifetimes in excess of six months. In this configuration, the volcano-style FI source has been shown to be an attractive alternative for the ionization and detection of many chemical species, including pesticides, gasoline and diesel fuels, incinerator combustion products, and explosives vapors.

To apply FI in the present instrument, we first needed to couple the volcano source with the ion trap. Since the ion trap typically produces ions within its internal volume, it was not designed to trap externally generated ions. Nonetheless, numerous examples exist of using external ion sources with a trap. In most cases, the ions are gated into the trap for a short time, thereby controlling the ion population. The actual trapping action is achieved through a combination of electrostatic effects (deceleration) and collisional damping by the helium buffer gas. The most effective means of injecting ions into the trap is to use a combination focus/steering lens system. Figure 24 shows the result of using the SIMION modeling program to design a suitable transfer lens system. The multielement extraction and steering lens arrangement allows ions whose initial trajectories are up to 20 degrees off axis to be focused through a 0.5-μm-diameter entrance aperture into the trap. The larger the collection cone, the higher the effective source efficiency. Not apparent in Figure 24 is the use of a four-quadrant steering lens element. By applying appropriate voltages to the four separate elements, it is possible to simultaneously focus and deflect the ions as necessary. The calculated optimum lens potentials are indicated in the figure.

The actual lens assembly that was fabricated as a result of the computer simulation is shown in Figure 25. The volcano FI source mount is visible on the right end of the lens stack, while the ion trap and continuous dynode electron multiplier is apparent on the other end. All the components are mounted on two parallel rails, allowing each portion to be aligned independently. Two quartz lamps mounted parallel to the rails are used to heat the entire assembly.

The assembly shown in Figure 25 was placed in a vacuum test stand where a variable pressure vapor generator was connected to the volcano source inlet. Appropriate electronics were assembled and connected to the system. These electronics supplied variable voltages to each of the lens elements, power for the source heaters, and control of the ion injection. The volcano source is


(a) Volcano before activation.

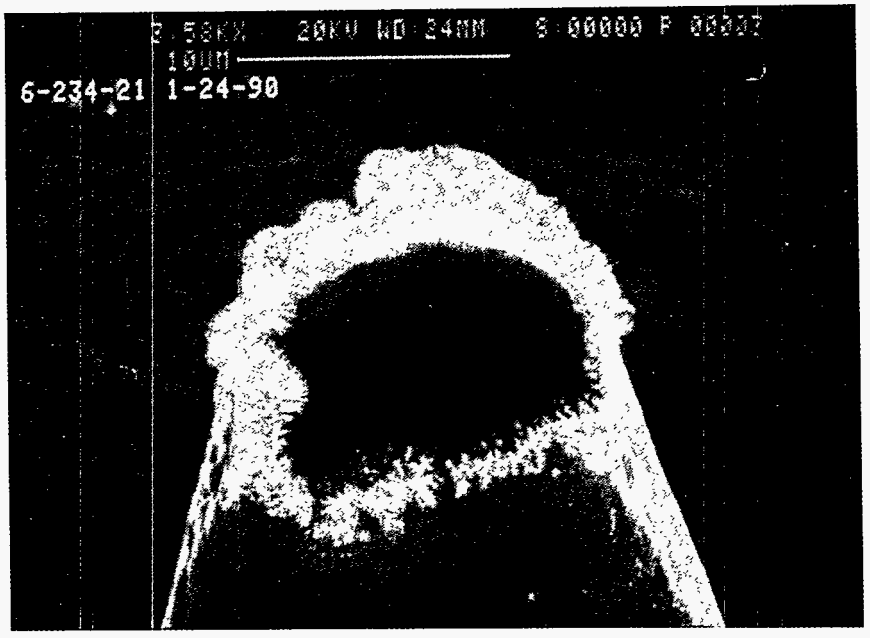


(b) Volcano after activation using a mixture of acetone, toluene, and butyl benzene.

RP-8074-8

Figure 23. Micrograph of volcano field ionization source.

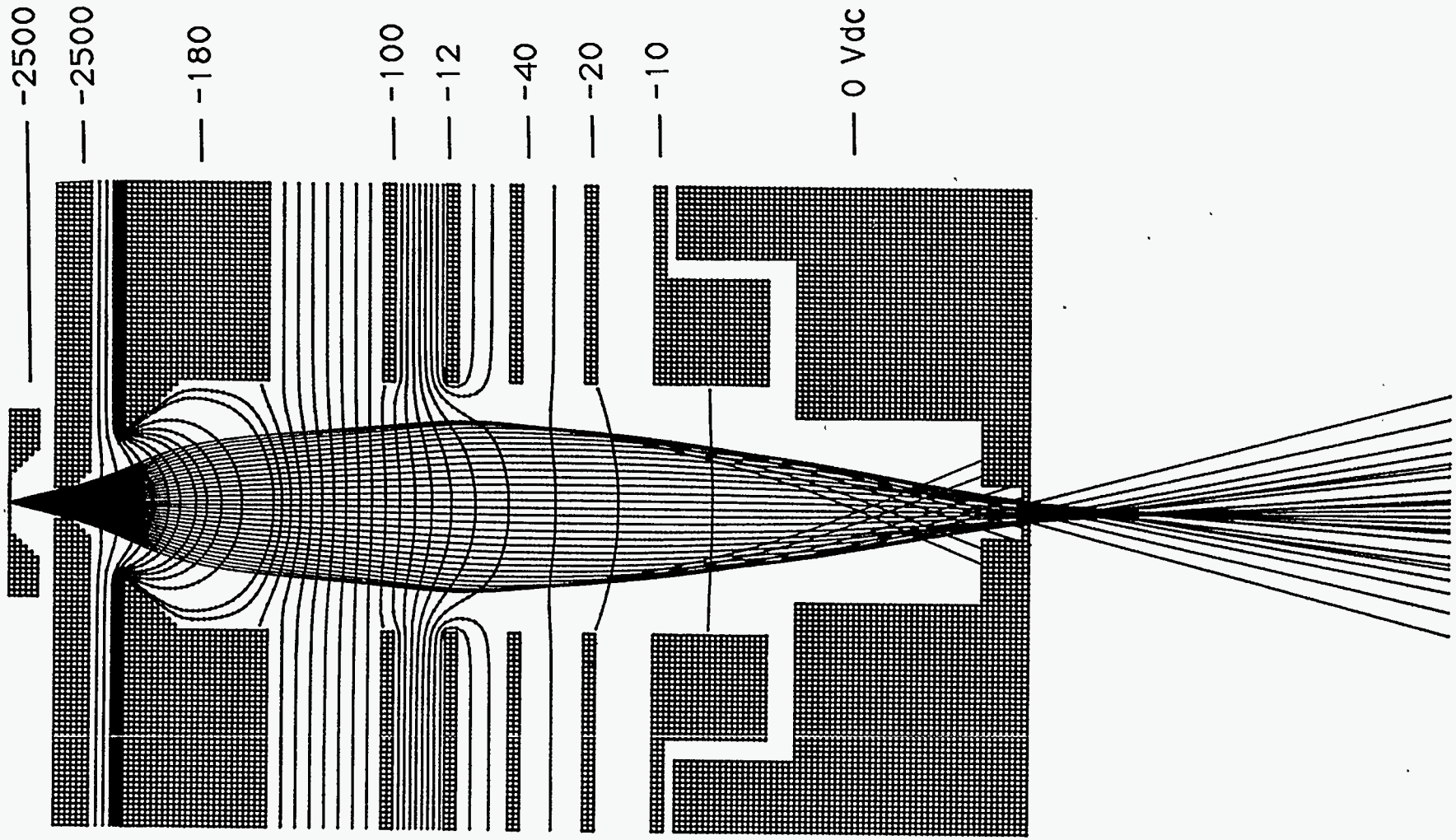


Figure 24. SIMION plot of volcano-ion trap lens interface.

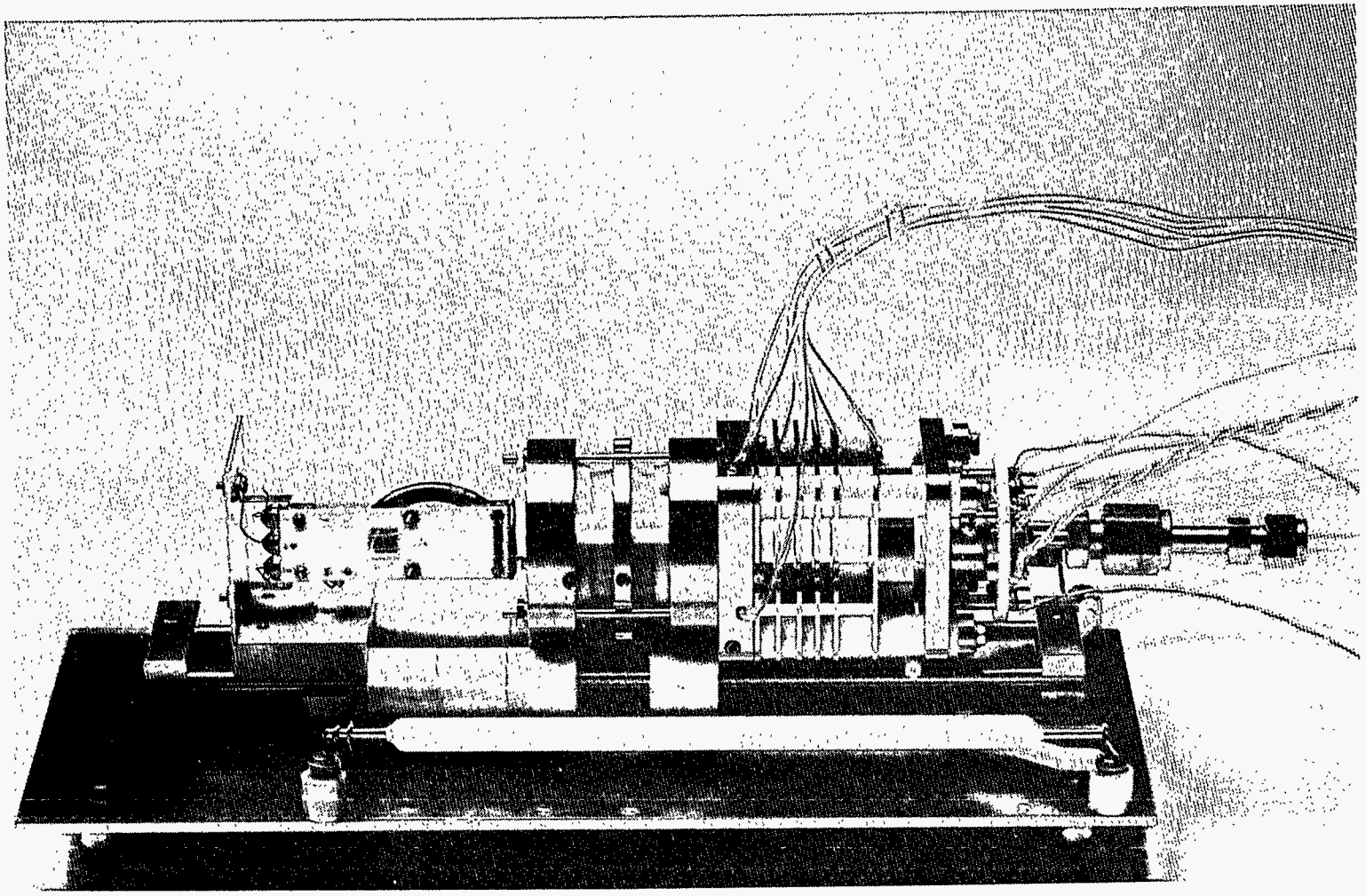

CP-4019-33

Figure 25. The ion trap equipped with a volcano field ionization source.

designed to run continuously rather than pulsing. Ion injection is controlled by gating the x-y steering elements to alternatively direct ions into the trap or deflect them away from the entrance aperture. The ion trap signal normally used to gate the electron ionization beam is instead used to gate the ions into the trap. The width of this ion injection pulse was variable from less than 10 μs to 25 ms.

### 3.2.10 Field Ionization Results

Figure 26 shows the preliminary results obtained using the volcano-FI equipped ion trap with a toluene vapor sample. The toluene pressure behind the volcano source was typically regulated at <1 Torr. As expected, the mass spectrum is dominated by the m/z 92 parent molecular ion species. The much weaker signal at m/z 93 corresponds to the presence of the naturally occurring carbon-13 isotope in about 1% of the toluene molecules. These data represent the first reported use of field ionization with a quadrupole ion trap mass spectrometer.

One of the more important operating parameters with an external ion source is the relative efficiency with which ions are captured within the trap volume. Several factors influence the trapping efficiency, including the injection energy and the buffer gas pressure. The helium buffer gas normally functions to collisionally cool ions formed within the trap volume so that they will remain trapped. The same collisional mechanism can also serve to slow injected ions sufficiently so that the electrostatic potentials within the trap can hold the externally produced ions.

Figure 27 shows the measured intensity of the toluene parent ion (m/z 92) as a function of the helium buffer gas pressure. At the normal operating pressure of 10 mTorr, the relative signal level is very small, indicating poor trapping. As the pressure is raised, the trapped ion signal rises more or less linearly up to a pressure of 10 to 11 Torr, before falling again. This behavior is most likely due to improved trapping as the pressure is increased until excessive ion loss results from scattering at the highest buffer gas pressures.

As noted above, the volcano source was operated continuously, while the ions were injected only over a narrow, variable-length, pulse. Figure 28 shows the variation of the trapping efficiency as the injection time is changed. For narrow injection pulses of 1-ms duration, the measured trapping efficiency is almost 8%. As the injection period is lengthened, the trapping efficiency drops smoothly and appears to level off at around 2% for injection times of 20 ms or more. Although the cause for this dependence is not obvious, it could be related to the absolute number of ions injected into the trap. Too many ions within the trap volume will cause significant distortions in the field potentials and hence alter the trapping capability of the system. For an instrument based on the combined volcano source-ion trap mass spectrometer, it will be necessary to determine the injection period that yields the optimum signal-to-noise ratio with the minimum limit of detection for the chemicals of interest.

One of the major advantages of using field ionization is its utility for the analysis of complex mixtures of organic vapors. Figure 29 shows a preliminary mass spectrum recorded using the volcano-FI source with the ion trap. The sample was a mixture of benzene, toluene, and ethyl benzene. Although the three components were present in the sample in equal amounts, their differing vapor pressures result in a gas phase composition that is not equal. The important feature to note in Figure 29 is that each organic compound gives rise to only one major ion peak corresponding to the parent $M^+$ species. Thus, benzene is represented by the m/z 78 peak, toluene by the m/z 92 peak, and ethyl benzene by the m/z 106 peak. In each case, the carbon-13 isotope peak is also apparent.

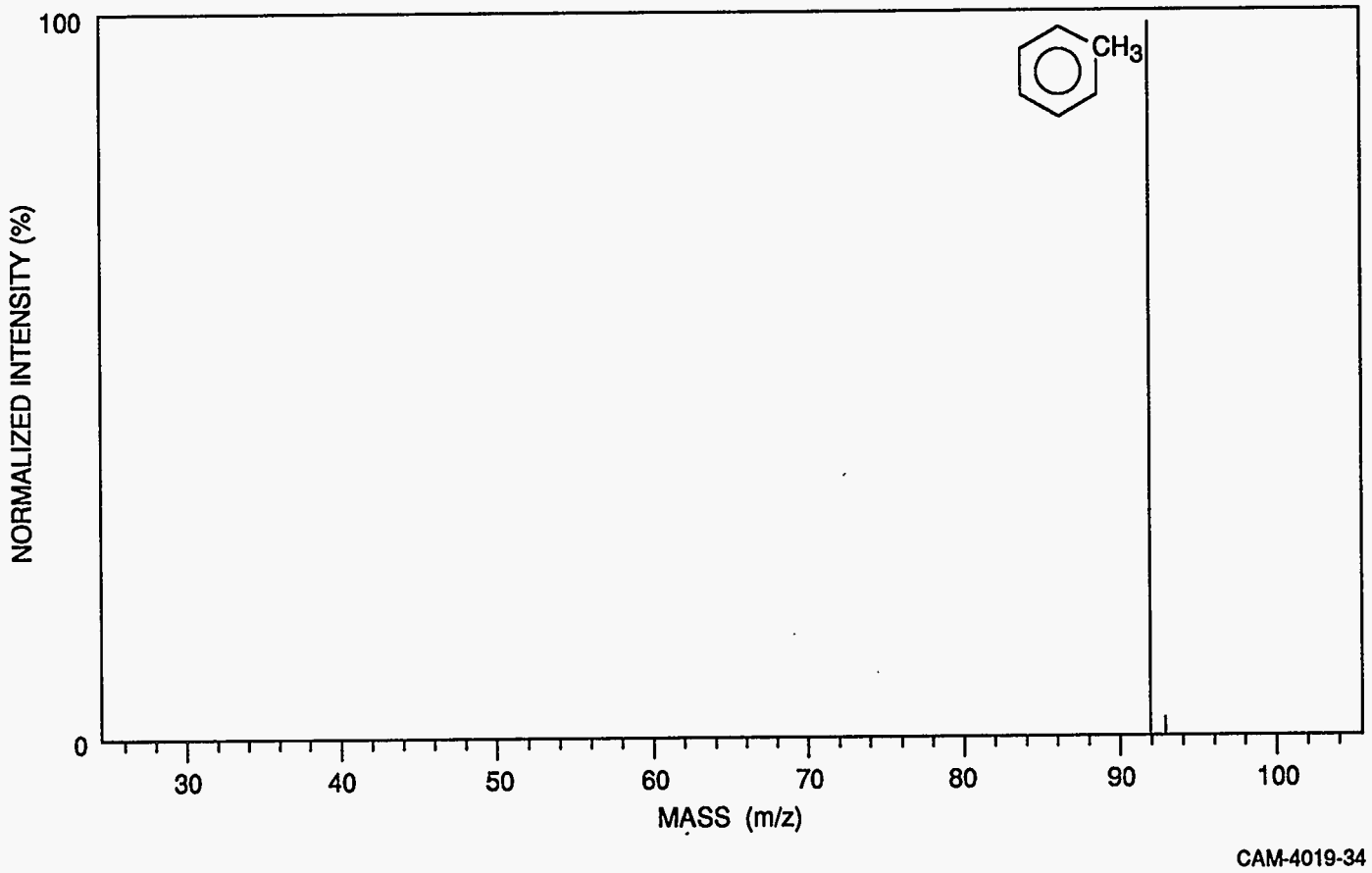


Figure 26. Field ionization mass spectrum of toluene recorded with the volcano-ion trap system.

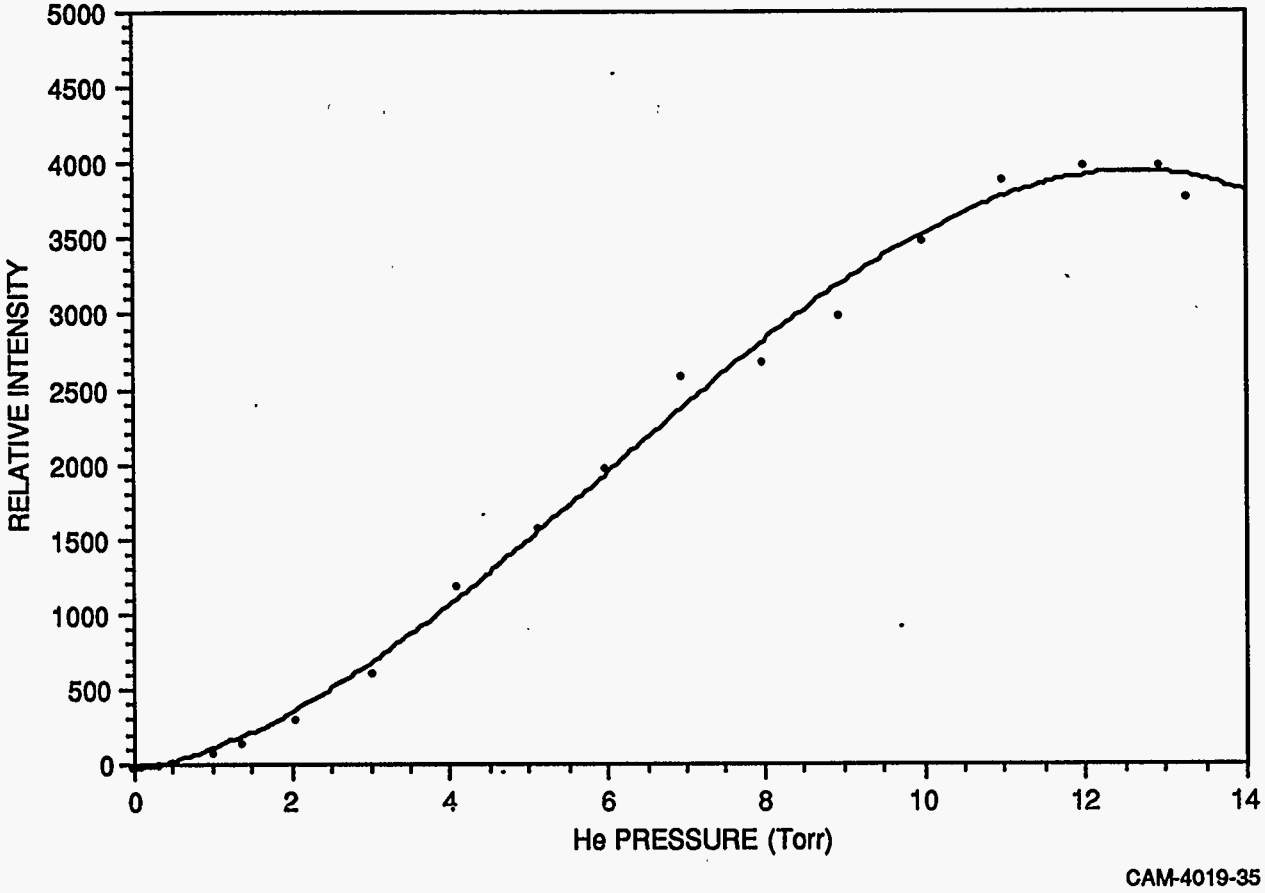


Figure 27. Effect of Helium buffer gas pressure on the trapping efficiency of toluene molecular ions (m/z 92).

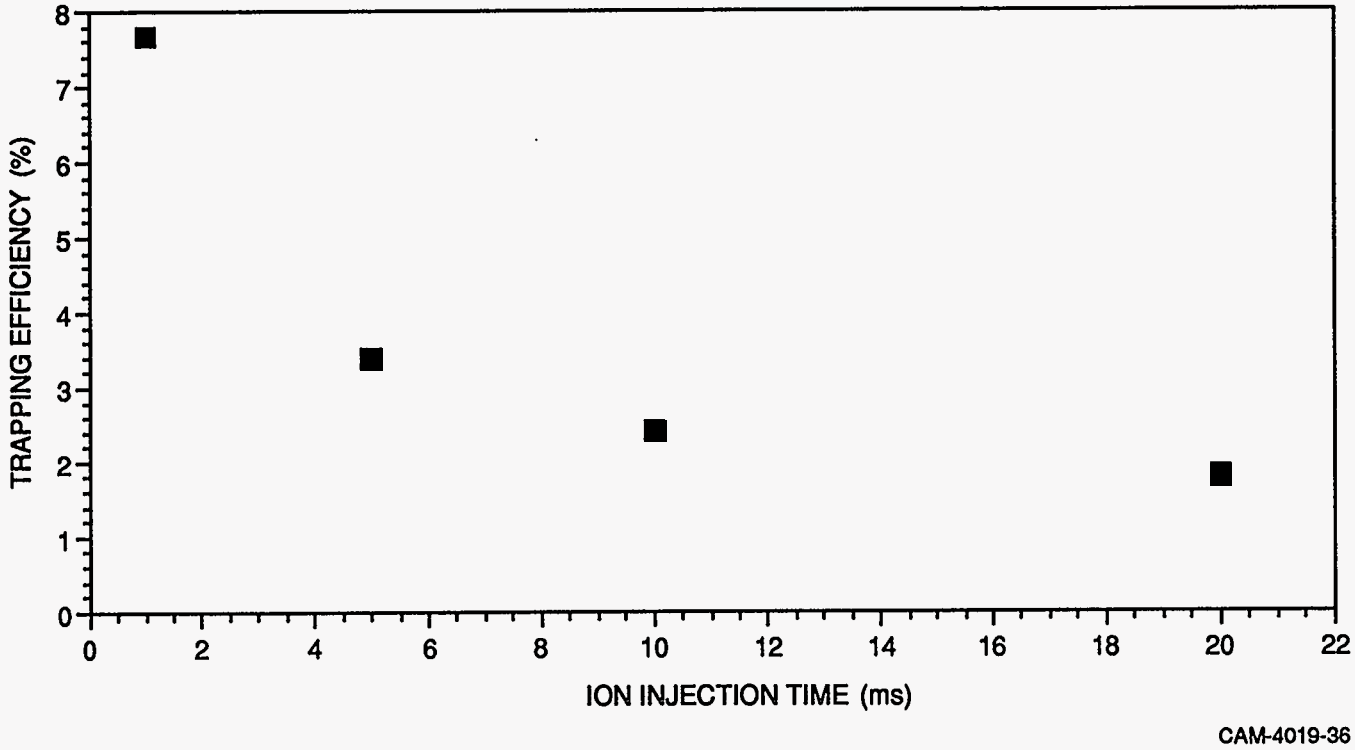


Figure 28. Trapping efficiency dependence for toluene molecular ions as a function of the ion injection time.

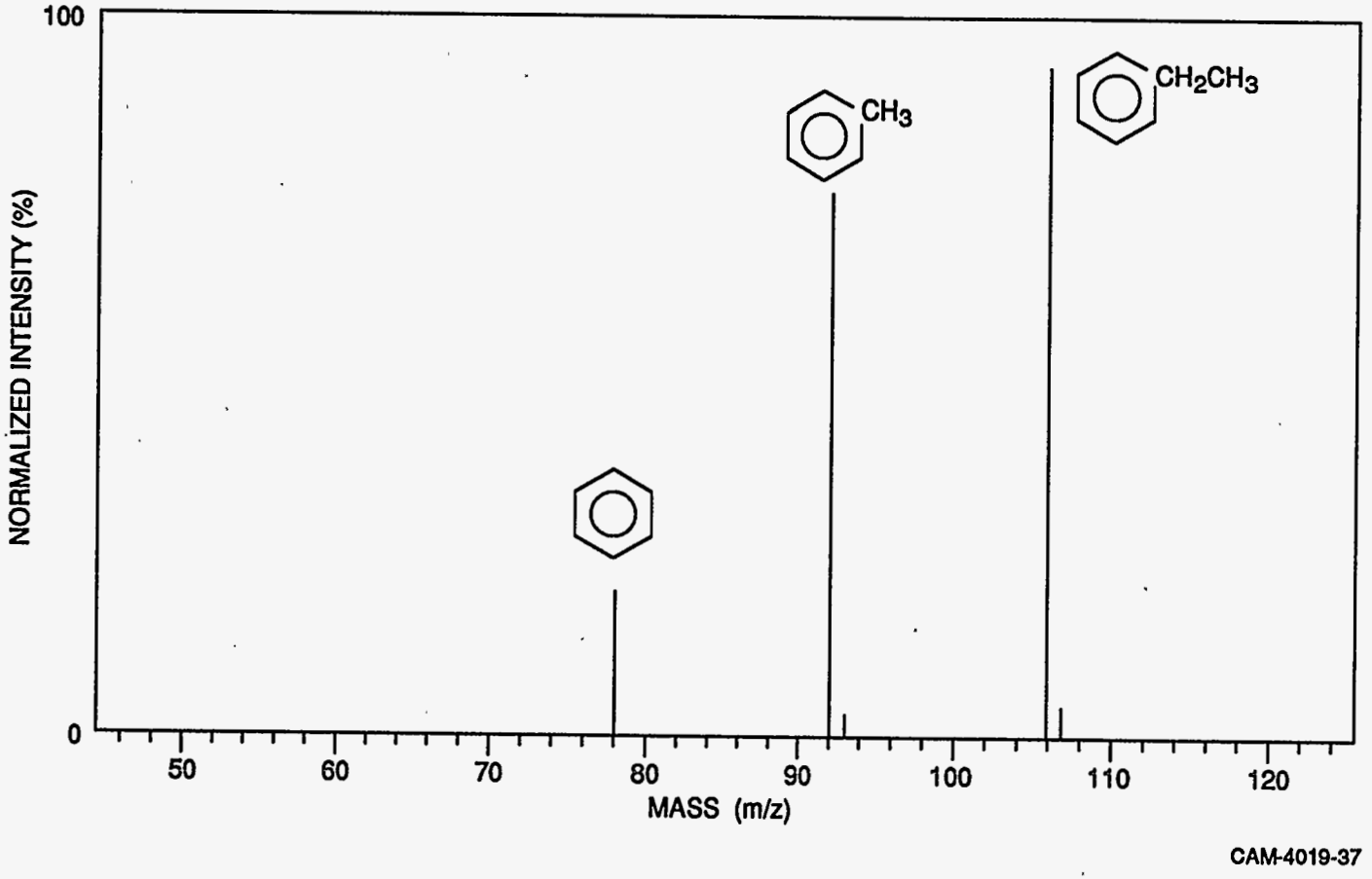


Figure 29. Field ionization mass spectrum of a mixture of volatile organics recorded with the volcano-ion trap system.

### 3.2.11 Inorganic Analysis Using Electron Ionization

As a part of the MARS program at PNL that is working toward developing instruments for the rapid characterization of the Hanford waste storage tanks, simulant samples have been prepared. These samples are nonradioactive, but contain a complex mixture of type the expected to be found in many waste storage tanks. PNL provided a small amount of the simulant sample to SRI for testing. Although the exact composition was not provided, the components include Na-ETDA, NaCl, Na phosphates, $NaNO_2$, $NaNO_3$, $NaCO_3$, NaF, NaOH, $Na_2SO_4$, nitrates of Cu, Cr, Fe, and Ni, KCl, and $CaCl_2$. The water-based paste formed from these materials has a pH in the 9-11 range.

Because we did not have enough time to investigate the transformation of the paste sample into a particulate sample by drying and milling, we instead chose to directly apply a small amount of material to the pyrolysis filament. The preloaded filament was then remounted on the ion trap end cap, and the entire assembly was placed under vacuum. Over a period of several minutes, the power applied to the pyrolysis filament was increased while mass spectra were continuously recorded. For heating currents below approximately 7 A, no appreciable vapor evolution was evident in the spectra. Above 7 A, several vapor "bursts" were observed, during which the mass spectra exhibited a number of strong peaks. Figure 30 shows a representative spectrum recorded with the filament at 9 A (filament temperature less than 900°C). Prominent peaks corresponding to water (m/z 18), sodium (m/z 23), $NO^+$ from nitrate (m/z 30), potassium (m/z 39), and $CO_2^+$ from carbonate (m/z 44) can be seen.

### 3.2.12 Light Scattering and Triggering

Because the laser light scattering system that is required to trigger data acquisition can also be used to optimize the particle beam alignment, we assembled the necessary optical components. The system is shown schematically in Figure 31. Initially, we used only the forward scattered channel to observe particles; however, a relatively high background signal (10-100 kHz count rate) prevented us from observing particles. We then reduced the background signal by careful masking of surfaces and the addition of optical baffles along the incident light path. Even with the background reduced by more than one order of magnitude, we did not observe particle induced light scattering.

To further reduce the background, we incorporated the back-scattered light signal in a coincidence configuration. By gating the counting electronics only when both channels measure a time coincident signal, the background signal rate should drop to near zero. Since the coincidence electronics are best adjusted with actual signals, we separated the instrument vacuum housing at the point where the laser light crosses the particle beam and attached a separate particle generator that directed a steady stream of (smoke) particles across the light path.

Once the electronics were adjusted (pulse height threshold and time coincidence window), the instrument was reassembled and tested with the normal particle beam generation system. The results of using various configurations are summarized in Table 15. The data reported in Table 15 confirm that the use of coincidence detection reduces the apparent signal level to less than 1 count/s despite a continuous signal rate 3 orders of magnitude higher. Conversely, in the presence of a particulate stream, the coincident signal level rises as a function of the particle density.

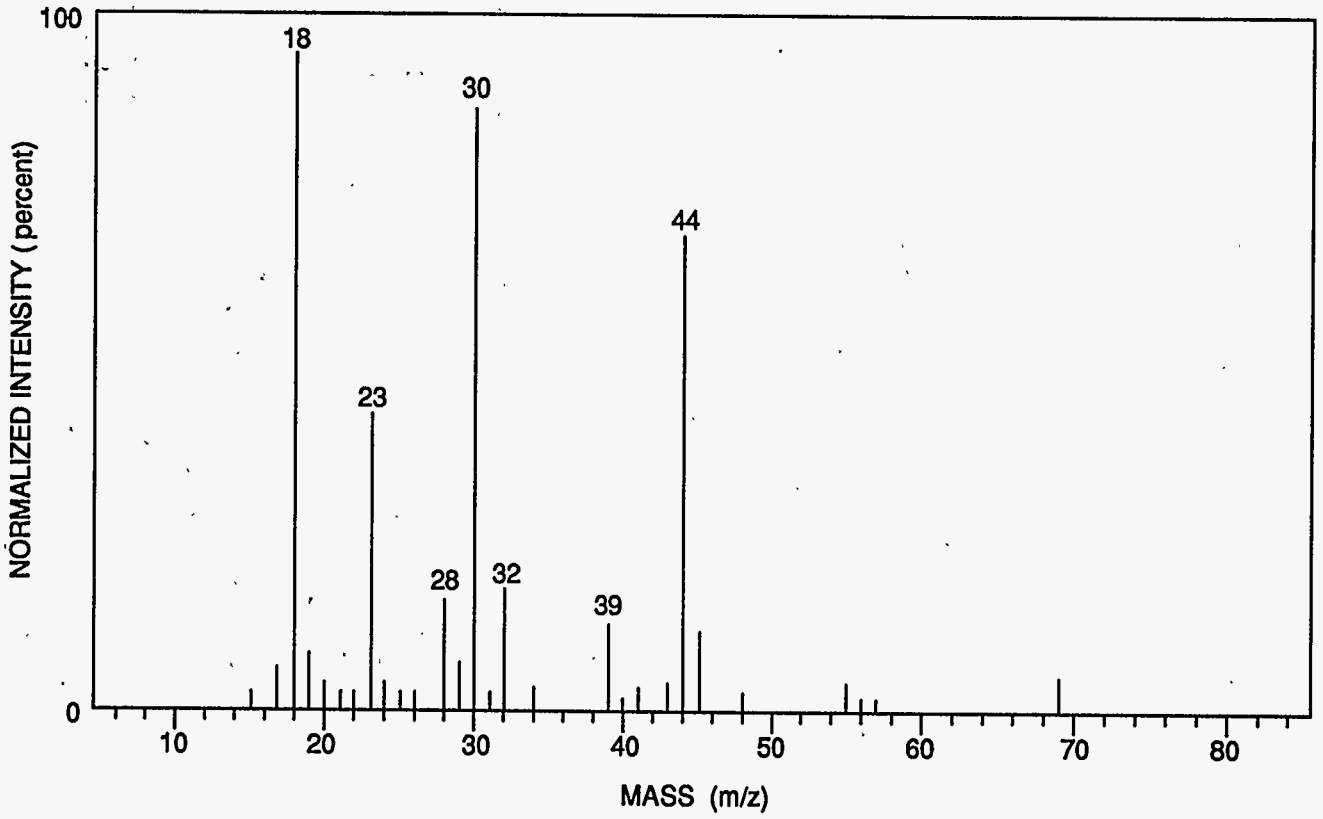


Figure 30. Ion trap mass spectrum of a simulated sample of inorganic salts from Hanford waste tanks. The sample was heated to 1000 °C.

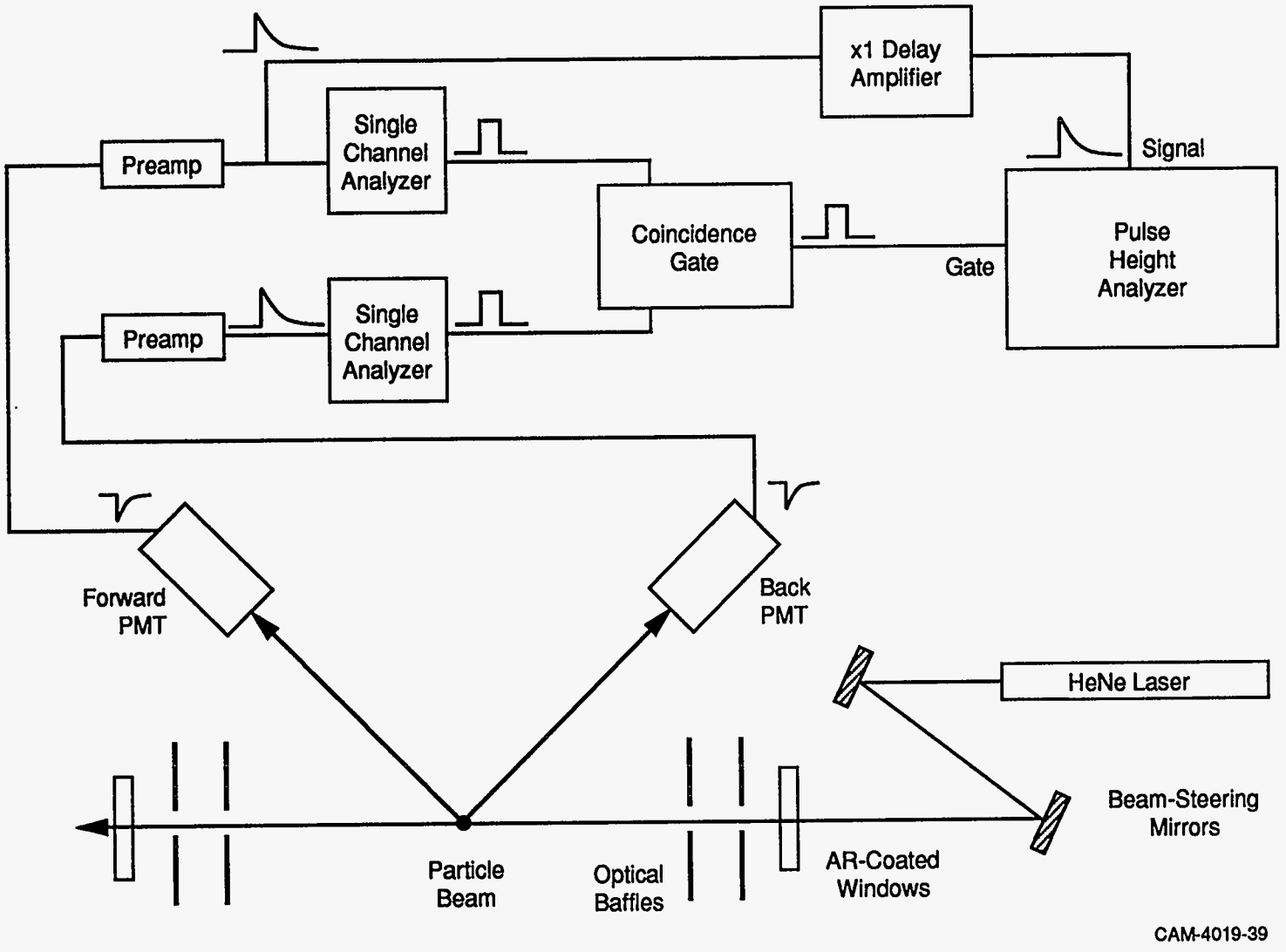


Figure 31. Optical and electrical schematic of the laser light scattering configuration.

**Table 15 Light Scattering Signal Levels**

| Configuration | Forward Signal (cts/10 s) | Back Signal (cts/10 s) | Coincidence (cts/10 s) |
|---|---|---|---|
| Background (no smoke particles, no laser light) | 4,839 | 1,584 | 4 |
| HeNe laser only | 5,843 | 2,582 | 6 |
| | 5,574 | 2,670 | 6 |
| Laser and smoke | 28,128 | 3,389 | 33 |
| (various | 43,791 | 3,904 | 87 |
| increasing | 126,827 | 7,386 | 546 |
| smoke | 236,597 | 10,727 | 1,024 |
| particle | 252,542 | 12,666 | 4,852 |
| levels) | 582,061 | 31,379 | 16,592 |

The development of a reliable and reproducible trigger signal is critical to the particulate analysis function. Once this trigger signal is available, appropriate modifications to the ion trap hardware/software will be required to initiate a mass analysis scan that is synchronized with the particle arrival and vaporization. Before having a particle trigger signal, we will allow the ion trap to operate in a free-run mode that is not synchronized with the particle arrival. The resulting mass spectra will represent an average of many particles rather than single particle spectra; however, the basic operation of the system will be verified. Although we have been in contact with a number of ion trap users, developers, and manufacturers, no one has yet been able to assist us in dealing with this problem. At present, the R&D group at Finnigan MAT will not release the source code that operates the ion trap, nor can they provide us with a customized version that allows triggering on command. We have located several individuals who have authorized copies of Finnigan's source code that they acquired in the course of performing cooperative research with the manufacturer. However, because of nondisclosure agreements, these individuals are also not in a position to release the code to us. They may, on the other hand, be able to provide us with the necessary customized software version.

A more attractive alternative is to work with another ion trap manufacturer. Of the two other current ion trap manufacturers, Varian and Teledyne, the latter has a reputation for working closely with outside research groups. Since they wrote all of their own source code, they could provide us with the necessary modifications. This course of action would require the purchase of an ion trap system from Teledyne. The Teledyne ion trap system actually offers improved operational capabilities and scan function flexibility that is not offered by either the Finnigan or Varian traps.

# 4 PHASE 1 STATUS

At the completion of the first phase of this research effort, the overall progress of the effort is behind schedule by several months, due primarily to numerous difficulties associated with particle sampling, transport, and introduction into the ion trap. Despite these difficulties, we have made significant technical progress in developing a real-time monitoring instrument for use by DOE. We have, for example, seen clear evidence for the detection of particulates that were externally generated and sampled, thus demonstrating the feasibility of this detection and characterization concept.

Before this technology can be tested further or developed into a fieldable prototype, several key challenges must be met. The most critical challenge is to develop a sampler that will deliver a representative vapor and particulate sample to the detector without significant size bias. Although samplers that use particulate entrainment in a gas stream similar to that proposed here have been described, their functionality and suitability for this instrument were found to be inadequate. Additional development work on this critical component is therefore required. Such a device would be applicable to any instrument that requires an extractive sampler for particulate and vapor delivery.

Once a sampler has been developed and demonstrated to provide the requisite sample, the next challenge is to introduce the particulates into the detector itself. Clearly, this is not a problem for the vapor sample, as demonstrated by the results presented in Sections 3.2.8–3.2.10. Introduction of micrometer-sized particles into an ion trap, however, may be more difficult. Because of the numerous electric fields in the vicinity of an operating ion trap mass spectrometer and the possibility that small particles will become electrostatically charged during sampling and transport, direct particle introduction into the trap may not be straightforward. Although methods are available to neutralize charged particulates, a more reasonable approach might be to relocate the pyrolysis filament external to the ion trap. This approach has the advantage of allowing the pyrolysis filament to be heated to higher temperatures without adversely affecting the operation of the trap. The primary disadvantage of an external pyrolysis filament is the need to transport the pyrolizate vapors into the trap without loss. Yet another approach that could be considered is the use of a different mass spectrometer, such as a conventional time of flight system. Time of flight mass spectrometers provide full scan spectra for each event with very good sensitivity and mass resolution.

The selection of a pyrolysis filament configuration and mass analyzer along with the development of a sampler would thus be the necessary tasks in the continued development of this instrument.

In our discussions with other DOE and national laboratory researchers, it is clear that the need for this instrument remains critical since new monitoring technologies have the highest priority. We are also not aware of any related efforts by others to develop an instrument with comparable capabilities. DOE headquarters continues to emphasize the need for high payoff/high risk technology development in the area of environmental waste management. We continue to view this project as having a high payoff, both for the original incinerator monitoring application, as well as the other applications described in Section 2.2.



☆U.S. GOVERNMENT PRINTING OFFICE: 1995 - 650-190/20004